ACS OMEGA

http://pubs.acs.org/journal/acsodf

Article

Metasurface Terahertz Perfect Absorber with Strong Multi-Frequency Selectivity

Qiangguo Zhou, Wanli Ma, Tuntan Wu, Yongzhen Li, Qinxi Qiu, Jiaxin Duan, Jingbo Li, Lin Jiang, Wei Zhou, Yanqing Gao, Jingguo Huang, and Zhiming Huang*

Cite This: *ACS Omega* 2022, 7, 36712−36727

Read Online

ACCESS | Metrics & More | Article Recommendations

ABSTRACT: In this paper, we design a metasurface terahertz perfect absorber with multi-frequency selectivity and good incident angle compatibility using a double-squared open ring structure. Simulations reveal five selective absorption peaks located at 0−1.2 THz with absorption 94.50% at 0.366 THz, 99.99% at 0.507 THz, 95.65% at 0.836 THz, 98.80% at 0.996 THz, and 86.70% at 1.101 THz, caused by two resonant absorptions within the fundamental unit (fundamental mode of resonance absorption, FRA) and its adjacent unit (supermodel of resonance absorption, SRA) in the structure, respectively, when the electric field of the electromagnetic wave is incident perpendicular to the opening. The strong frequency selectivity at 0.836 THz with a *Q*-factor of 167.20 and 0.996 THz with a *Q*-factor of 166.00 is due to the common effect of the FRA and SRA. Then, the effect of polarized electromagnetic wave modes (TE and TM modes) at different angles of incidence (θ) and the size of the open rings on the device performance is analyzed. We find that for the TM mode, the absorption of the resonance peak changes only slightly at θ = 0−80°, which explains this phenomenon. The frequency shift of the absorption peaks caused by the size change of the open rings is described reasonably by an equivalent RLC resonant circuit. Next, by adjusting two-dimensional materials and photosensitive semiconductor materials embedded in the unit structure, the designed metasurface absorber has excellent tunable modulation. The absorption modulation depth (MD) reaches ≈100% using the conductivity of photosensitive semiconductor silicon ($\sigma_{SI\text{-}ps}$), indicating excellent control of the absorption spectrum. Our results can greatly promote the absorption of terahertz waves, absorption spectrum tunability, and frequency selectivity of devices, which are useful in the applications such as resonators, bio-detection, beam-controlled antennas, hyperspectral thermal imaging systems, and sensors.

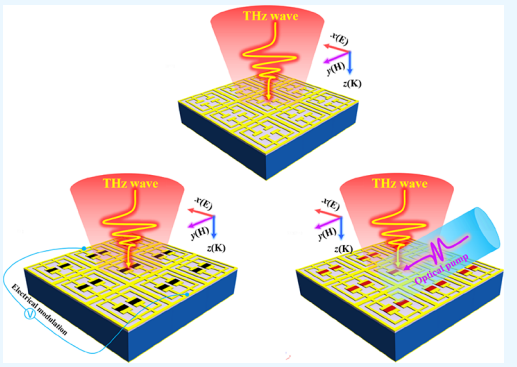

1. INTRODUCTION

Terahertz (THz) radiation is in the range of 0.1−10 THz (1 THz = 10^{12} Hz) between infrared and microwaves in the electromagnetic spectrum. With the rapid development of THz science and technology, it shows broad applicational prospects in many fields, such as physics, biology, electronic information technology, life sciences, materials science, radar, and security detection. The metasurface is an artificial composite structure periodically arranged by an array of sub-wavelength structural units. Metasurfaces can achieve unique properties, such as negative permittivity, negative permeability, a negative refractive index, an inverse Doppler effect, and inverse Snell's law through artificial design.[1−5] These unique electromagnetic properties of the metasurface have attracted widespread attention. The metasurface absorber can achieve high absorption of THz waves and currently shows great applicational potential in medicine, biology, and aerospace exploration.[6−11] In 2008, Landy et al. designed a metasurface device capable of perfect absorption, which consists of a surface metal resonator, a polyimide dielectric layer, and a bottom metal strip.[12,13] The results showed that the absorptance was above 99% at 11.48 GHz. The absorber had high absorptance and a small unit size, but its absorption frequency band was narrow, and it was very sensitive to the polarization direction of electromagnetic waves. To solve this problem, Landy et al. designed a symmetrical absorber structure.[14] The simulation results showed that the absorptance of the metamaterial absorber structure reached 95% at 1.13 THz. The THz metasurface absorber designed by Hu et al.[15] was also composed of three layers of a surface metal resonator, a middle polyimide dielectric layer, and a bottom metal strip. Experimental results showed that the maximum absorptance of the absorber could reach 70%. In 2009, Wen et al. proposed a

Received: August 6, 2022
Accepted: September 23, 2022
Published: October 5, 2022

dual-frequency absorber in the THz band.[16] The bottom layer of the absorber was a continuous metal film, the dielectric isolation layer polyimide, and the top layer was an artificial unit structure. The absorptance was above 99.99% at 0.5 and 0.94 THz. Janneh et al. report on a novel high Q-factor dual-band THz perfect absorber composed of a metasurface located on top of a flexible polyimide spacer deposited on a silver ground layer.[17] The simulation showed that at f_1 = 1.80 THz and f_2 = 2.26 THz, the Q-factors are $Q(f_1)$ = 120 and $Q(f_2)$ = 94 and the absorption coefficients are $A(f_1)$ = 99.8% and $A(f_2)$ = 99.6%, respectively. Xu et al.[18] embedded the photosensitive material silicon into the basic unit structure of the metamaterial and achieved a broadband red shift of the resonance peak of the absorption spectrum from 1.17 to 0.68 THz and a broadband blue shift of the absorption frequency from 0.68 to 1.41 THz by changing the electrical conductivity of the photosensitive silicon with an absorptance of 98%. Zhang et al.[19] achieved multi-band tunable absorption by superimposing two rectangular and two circular metallic resonant cavities with proper placement of photosensitive semiconductor silicon in different critical regions, respectively. However, the multi-band tunable metasurface absorber is complex in structure, inconvenient in fabrication, and low in absorption, which cannot achieve the effect of perfect absorption.

The above work shows that the metasurface THz absorber had fewer absorption peaks, and it was difficult to achieve three or more absorption peaks. Moreover, it was sensitive to the angle of incidence of electromagnetic waves. In addition, the above work could not achieve a high Q-factor and the frequency selectivity was poor, which limited its application in the fields of sensing and selective thermal imaging.

We design a metasurface THz multi-frequency perfect absorber with strong frequency selectivity and good incidence angle compatibility. Applying the principle of impedance matching and electromagnetic resonance theory, the reason why the metasurface THz absorber could achieve high-efficiency absorption is explained herein, providing a theoretical basis and research direction for the development of metasurface THz absorbers. We find two different electromagnetic dipole resonance absorption phenomena caused by the fundamental mode of resonance absorption (FRA) and the supermodel of resonance absorption (SRA). By designing structures with both FRA and SRA, metasurface devices with strong frequency selectivity can be realized, providing an important theoretical basis for the development of metasurface THz absorbers in the fields of sensing and resonators. In addition, we explain the new absorption phenomena arising from the change in the opening size by using the equivalent RLC circuit model. By embedding 2D materials and photosensitive semiconductor silicon into the unit structure, a metasurface THz absorber with excellent tunable characteristics has been realized. Simulation experiments show that at 0.967 THz, the absorption MD > 62.17% by tuning the Fermi level (E_f) of graphene; tuning $\sigma_{SI\text{-}ps}$ achieved an MD > 99.99% (≈100%) at 0.504 and 0.887 THz. The designed tunable metasurface absorber has an obvious modulation effect and strong tunable characteristics, which greatly expand the applicational potential of the THz absorber in modulators, detectors, sensors, and hyperspectral thermal imaging systems.

2. THEORETICAL ANALYSIS

2.1. Absorptance. Absorptance refers to the ratio of the electromagnetic radiation energy absorbed by the measured object to the incident electromagnetic radiation energy. For metasurface absorbers, the absorptance and absorption bandwidth are important indicators to measure absorption performance.[20,21] The higher the absorptance, the better the light response performance of the absorber. If the reflectance, transmittance, and absorptance are, respectively, $R(\omega)$, $T(\omega)$, and $A(\omega)$, the absorptance of the absorber can, thus, be expressed as

$$A(\omega) = 1 - R(\omega) - T(\omega) \tag{1}$$

In the finite element method, the S-parameter is a network parameter based on the relationship between the incident and reflected waves, which is suitable for microwave circuit analysis to describe the circuit network in terms of the reflected signal at the device port and the signal transmitted from the port to the other port (see Figure 1)

$$S_{11} = \frac{b_1}{a_1} = \frac{V_{\text{reflected at port 1}}}{V_{\text{incident port 1}}} |S_{11}| = \frac{\text{Ap}_{(V_{\text{reflectedatport1}})}}{\text{Ap}_{(V_{\text{incidentport1}})}} \tag{2}$$

$$S_{21} = \frac{b_2}{a_1} = \frac{V_{\text{out of port 2}}}{V_{\text{incident port 1}}} |S_{21}| = \frac{\text{Ap}_{(V_{\text{out of port 2}})}}{\text{Ap}_{(V_{\text{incident port 1}})}} \tag{3}$$

$$S_{22} = \frac{b_2}{a_2} = \frac{V_{\text{reflected at port 2}}}{V_{\text{incident port 2}}} |S_{22}| = \frac{\text{Ap}_{(V_{\text{reflected at port 2}})}}{\text{Ap}_{(V_{\text{incident port 2}})}} \tag{4}$$

$$S_{12} = \frac{b_1}{a_2} = \frac{V_{\text{out of port 1}}}{V_{\text{incident port 2}}} |S_{12}| = \frac{Ap_{(V_{\text{out of port 1}})}}{Ap_{(V_{\text{incident port 2}})}} \tag{5}$$

S_{11} and S_{21} in the S-parameter can be used to represent $R(\omega)$ and $T(\omega)$, respectively

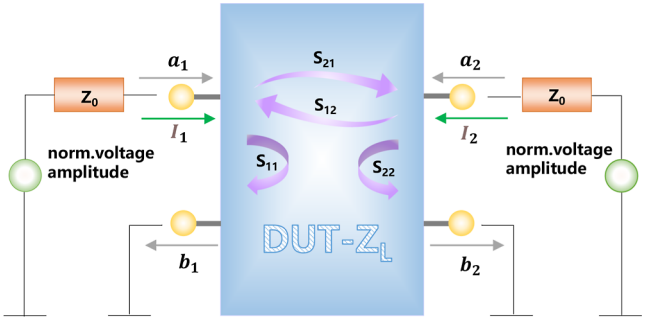

Figure 1. S-parameters are defined under the condition that the transmission line is terminated at both ends, and the general transmission line characteristic impedance Z_0 = 50 ohm. Therefore, when Z_0 is defined differently, the S-parameter values are not the same, that is, S-parameters are based on the results obtained under a specified Z_0 condition, $S_{ij}(\text{dB}) = \frac{\text{port}(i)_{\text{reflected or out}}}{\text{port}(k)_{\text{incident}}} = 20\log|S_{ij}|$. Ap is the voltage amplitude. Z_L is the load impedance. S_{11}, when port 2 is matched, the reflection coefficient of port 1, that is, the return loss; S_{21}, when port 2 is matched, the forward transmission coefficient from port 1 to port 2, that is, the insertion loss; S_{22}, when port 1 is matched, the reflection coefficient of port 2; S_{12}, when port 1 is matched, the reverse transmission coefficient from port 2 to port 1.

https://doi.org/10.1021/acsomega.2c05016
ACS Omega 2022, 7, 36712−36727

$$R(\omega) = |S_{11}|^2 \tag{6}$$

$$T(\omega) = |S_{21}|^2 \tag{7}$$

The degree of impedance matching of the material and the free space determines the size of S_{11} (or $|S_{11}|$). If a perfect match of the material and the free space can be achieved, this can then be regarded as the electromagnetic wave that completely enters the material without reflection, and at this time, $|S_{11}| \approx 0$; the loss of electromagnetic waves in the material determines the size of $|S_{21}|$; the greater the loss, the smaller the $|S_{21}|$. The above analysis shows that when the metasurface absorber reaches impedance matching, perfect absorption of $A(\omega) \approx 1$ can be achieved.

2.2. Principle of Impedance Matching. Metasurface devices generally interact with incident electromagnetic waves using electrical resonance or magnetic resonance.[12,22] To have these two resonance modes at the same time, a metasurface device usually consists of three layers: the top layer is usually a structural layer composed of metallic or semimetallic metamaterials; the middle layer is a dielectric layer; and the bottom layer is generally a metal layer, usually a metallic thin film or a metallic grid array. The uppermost structural layer and the intermediate dielectric layer produce a polarization charge distribution under the action of an electric field, that is, an electric resonance response. Because the top and bottom layers are both metals, they can generate a polarized current under the action of an electromagnetic field, and the polarized current generates a polarizing magnetic field, which couples with the incident magnetic field to produce a magnetic resonance response.[19,23,24] The electromagnetic response degree of the metamaterial structure can be expressed by the equivalent electrical conductivity and magnetic permeability of the structural unit. These two equivalent parameters can be controlled by adjusting the thickness of the structural medium layer and the material properties. Assuming that the impedance of the free space is Z_0 (characteristic impedance), the equivalent impedance of the metasurface absorber is Z_L (load impedance), see Figure 1, and the reflection coefficient can be expressed as[10]

$$r(\omega) = \frac{Z_L - Z_0}{Z_L + Z_0} \tag{8}$$

$$A(\omega) = 1 - R(\omega) - T(\omega) \approx 1 - r(\omega)^2 = 1 - \left|\frac{Z_L - Z_0}{Z_L + Z_0}\right|^2 = 1 - \left|\frac{\sqrt{\varepsilon_0\mu_1} - \sqrt{\varepsilon_1\mu_0}}{\sqrt{\varepsilon_0\mu_1} + \sqrt{\varepsilon_1\mu_0}}\right|^2 \tag{9}$$

where $Z_0 = \sqrt{\mu_0/\varepsilon_0}$, $Z_L = \sqrt{\mu_1/\varepsilon_1}$, and $T(\omega) \approx 0$. From eqs 8 and 9, it can be seen that if the metasurface absorber has a higher absorptance, Z_L should be close to Z_0, $Z \approx Z_0$, $\mu_0/\varepsilon_0 \approx \mu_1/\varepsilon_1$, and $\sqrt{\varepsilon_0\mu_1} - \sqrt{\varepsilon_1\mu_0} \approx 0$; that is, the equivalent impedance is close to the free space impedance at this time and $R(\omega) \approx 0$. If the thickness of the metal layer at the bottom of the absorber structure is greater than the skin depth of the THz wave in the metal at this time,[25] $T(\omega) \approx 0$ and the energy of the incident wave is localized in the interior of the metamaterial and at the interface interacting with the metamaterial to produce electric field resonance and magnetic field resonance so that most of the electromagnetic field energy of the incident wave is absorbed by the metasurface structure, and a metasurface perfect absorber is, thus, formed.[26]

3. STRUCTURAL DESIGN AND RESULT ANALYSIS

3.1. Structure and Design. In the THz band, the skin depth δ of metals can be expressed as

$$\delta = \sqrt{\frac{1}{\pi f \mu \sigma}} \tag{10}$$

where f is the frequency of electromagnetic waves; σ is the conductivity of the metal; $\mu = \mu_0\mu_r$, the permeability; $\mu_0 = 4\pi \times 10^{-7}$ N/A^2, the vacuum permeability; and μ_r, the relative permeability. For silver (Ag), copper (Cu), gold (Au), aluminum (Al), platinum (Pt), and other metal materials, $\mu_r \approx 1$, and the skin depth of these metal materials in the THz band was calculated according to the above formula, as shown in Figure 2, where it can be seen that the skin depth of THz

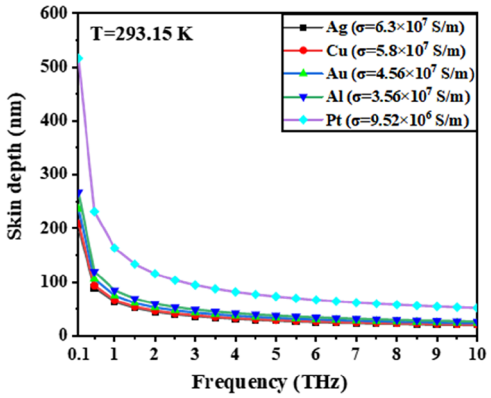

Figure 2. Skin depth of THz wave for different metal materials.

waves for Au materials was basically maintained below 100 nm in the THz band. Therefore, the thickness of the underlying Au is 100 nm, greater than the skin depth of THz platinum for the gold material, so that $T(\omega) \approx 0$ ensured the efficient absorption of THz waves by the metasurface absorber.

The structure of the metasurface absorber is shown in Figure 3. It consisted of four layers, with the top layer being a

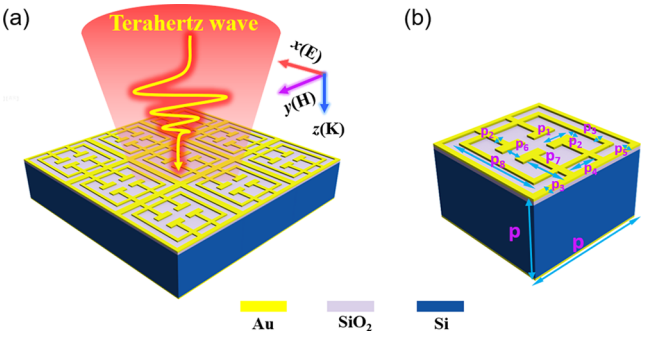

Figure 3. Schematic diagram of the structure of the THz absorber: (a) structural schematic of the proposed metasurface absorber and (b) unit structure.

metasurface structure. The material used for the top metasurface was gold, and the conductivity $\sigma_1 = 4.561 \times 10^7$ S/m, with a thickness of 300 nm. The second layer was made of silicon dioxide material, the conductivity $\sigma_2 = 10^{-18}$ S/m, and the dielectric constant $\varepsilon_1 = 3.9$, with a thickness of about 300 nm. The third layer was made of silicon material, the conductivity $\sigma_3 = 2.5 \times 10^{-4}$ S/m, and the dielectric constant $\varepsilon_2 = 11.9$, with

https://doi.org/10.1021/acsomega.2c05016
ACS Omega 2022, 7, 36712−36727

a thickness of about 100 μm. The bottom layer was made of gold material, and the conductivity was σ_1, with a thickness of 100 nm. The metasurface structure on the top layer consisted of two split resonant ring structures and two square rings. Other specific parameters of the structure were P = 100 μm, P_1 = 20 μm, P_2 = 6 μm, P_3 = 4 μm, P_4 = 28 μm, P_5 = 9 μm, P_6 = 10 μm, P_7 = 35 μm, and P_8 = 72 μm.

3.2. Simulation Results and Discussion. High Frequency Structure Simulator (HFSS) software was used for the simulation experiments. This software is three-dimensional (3D) electromagnetic simulation software based on the principle of the finite element method (FEM), which can provide an effective and fast solution for 3D electromagnetic field simulation. This periodic structure is simulated by using master-slave boundary conditions, Floquet excitation, and adaptive mesh dissection techniques. The basic process (running process) of the FEM for solving the problem consists of three parts: discretization of the analysis object, finite element solution, and processing of the calculation results. The absorption spectrum of the absorber at 0−1.2 THz was simulated and is shown in Figure 4. Since the thickness of the

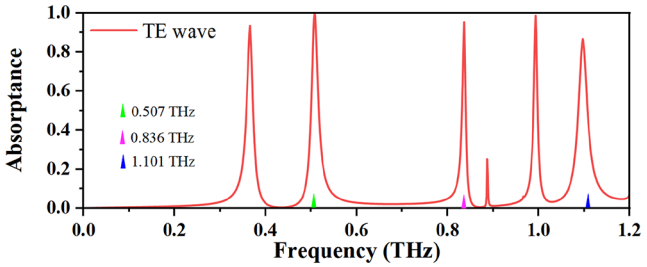

Figure 4. Absorption spectrum of the metasurface THz absorber (TE wave, the electric field of the electromagnetic wave is perpendicular to the opening, vertically polarized wave) at 0−1.2 THz.

underlying metal film was much larger than the skin depth of the THz wave, $T(\omega) \approx 0$. Simulation experiments show the presence of five absorption peaks here: $A(f_0$ = 0.366 THz) = 94.50%, $A(f_0$ = 0.507 THz) = 99.99%, $A(f_0$ = 836 THz) = 95.65%, $A(f_0$ = 0.996 THz) = 98.80%, and $A(f_0$ = 1.101 THz) = 86.70%, when the electric field direction of the electromagnetic wave is perpendicular to the opening.

The appearance of the absorption peak is mainly due to the mutual electromagnetic coupling between the upper and lower surfaces of the absorption structure under the action of incident electromagnetic waves. This can be specifically explained by magnetic resonance theory. To better explain the magnetic resonance theory, the metal strip structure is used to explain the changes between the internal parts of the metasurface and the roles played by different parts after the electromagnetic wave is irradiated to the metasurface so that the direction of the electric field of the incident electromagnetic wave is consistent with the direction of the long axis of the structural metal when the incident wave irradiates the surface of the absorber structure, the metal strip will be in the electric field consistent with the direction of the long axis under the action of the electromagnetic field, and the charge in the metal strip will be gathered at the ends of the strip structure[27] (see Figure 5). Because the charges can be induced by each other, the accumulation will not be confined to the metal strips on the top layer. The charges accumulated on the top layer will have a strong electromagnetic coupling effect with the bottom metal layer so that the bottom metal layer induces a charge distribution opposite to that of the top layer. The two ends of the metal strip accumulate charges of different properties, so a directional current will be generated inside the metal strip. The properties of the charges accumulated on the top metal strip and the bottom metal plate are opposite, leading to the opposite direction of the current generated by the upper and lower layers. Figure 5b presents the distribution of the induced magnetic field and induced electric field at the top and bottom layers of the structure.[28] First, the charges of different properties appearing in the upper and bottom structures can be regarded as countless electric dipoles, resulting in electric dipole resonance. Second, the antiparallel currents generated by the upper and lower structural structures formed magnetic dipoles inside the absorber, resulting in magnetic dipole resonance. Because the surface current is mainly distributed on the upper and lower metal planes, the induced magnetic field distribution will be mainly concentrated in the middle dielectric layer of the absorber structure, and the resonance absorption will be formed through the magnetic dipole resonance. The co-frequency generation of electrical and magnetic resonance allows the metasurface absorber to absorb almost 100% of the electric and magnetic field energy of the incident electromagnetic wave at the resonant frequency point. The thickness of the dielectric layer in the metasurface absorber determines the coupling of electric dipoles, magnetic dipoles, and electromagnetic resonance; that is, the absorptance of the absorber can be adjusted by optimizing the thickness of the dielectric layer.

The resonance absorption spectrum shows that the resonance peaks at 0.836 and 0.996 THz are sharper than the other resonance peaks. The sharper the resonance peak is,

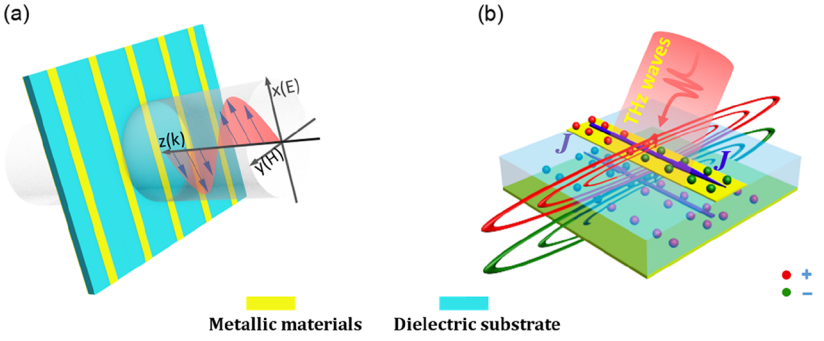

Figure 5. Schematic diagram of the metasurface absorber: (a) schematic diagram of the periodic structure and the unit structure and (b) distribution diagram of the induced electric field and magnetic field and distribution diagram of induced current.

https://doi.org/10.1021/acsomega.2c05016
ACS Omega 2022, 7, 36712−36727

the stronger frequency selective it is. Usually, the value of the absorptance on both sides of the resonant peak is equal to the maximum absorptance at the frequency of $1/\sqrt{2}$ width for the frequency bandwidth, that is, $\Delta f = f_2 - f_1$, with f_1 and f_2 at the absorption strength $I_{f_1} = I_{f_2} = I_{f_0}/\sqrt{2}$. The higher Q-factor (quality factor, $Q = f_0/\Delta f$) indicates that the resonant peak is sharper, and the frequency selection of the device is stronger. The high Q-factor indicates that this device can be used in sensors with frequency selectivity.[29] The Δf, Q-factors, and absorption modes at different resonant frequency points are listed in Table 1. The following is a further analysis of the

Table 1. Δf and Q-Factors at Different Resonant Frequency Points

f_0 (THz)	f_1 (THz)	f_2 (THz)	Δf(THz)	Q-factors	absorption modes
0.366	≈0.360	≈0.371	0.011	33.27	FRA
0.507	≈0.500	≈0.513	0.013	39.00	FRA
0.836	≈0.833	≈0.838	0.005	167.20	FRA + SRA
0.996	≈0.993	≈0.999	0.006	166.00	FRA + SRA
1.101	≈1.093	≈1.110	0.017	64.76	SRA

device with different frequency selectivity at different resonance peaks to provide theoretical support for the development of THz metasurface absorption devices with high frequency selectivity.

In Figure 6, the surface electric field intensity, magnetic field intensity, and current density distribution at 0.507 THz (Δf = 0.013, Q = 39.00) and 1.101 THz (Δf = 0.017, Q = 64.76) were simulated. From the analysis of the absorption spectrum, it can be seen that the THz wave of a specific frequency could be absorbed efficiently when entering the metasurface absorber, forming an absorption peak, but different parts of the structure contribute differently to absorption, so different metasurface materials and structures produce different absorption properties. The THz wave used was a TE wave (the electric field of the electromagnetic wave is perpendicular to the opening, see Figure 3a), and the distribution of the electric charge could be inferred from the distribution of the electric field intensity, and the electric charge moved along the metal strip. The color bars in the text have already normalized. At 0.507 THz, the electric field was mainly distributed at the open ring within the unit structure; that is, the absorption peak was mainly generated by the electromagnetic dipole resonance absorption formed by the split ring and the underlying metal film. At 1.101 THz, the electric field was mainly distributed around square Ring 1 and between the adjacent unit structures. The absorption peaks here were mainly generated by the electromagnetic dipole resonance coupling of adjacent structural units, which was a new coupling mode (see Figure 6d–f). The surface current defined here is the surface current density (J_s), that is, the product of the surface current density element of the carrier (ρ_s) and the carrier drift velocity (ν)

$$\boldsymbol{J_S} = \rho_s \boldsymbol{\nu}\ (A/m) \tag{11}$$

At 0.507 THz, the current on the upper surface of the absorber structure was mainly concentrated on the middle square metal ring (Ring 2), exactly opposite to the current direction corresponding to the bottom layer of the absorber structure (see Figure 6c). This is because when an electromagnetic wave is an incident on the surface of the structure, the charge gathered on the top layer will have a coupling effect with the bottom metal film under the action of the electromagnetic wave, and a charge distribution opposite to the top layer will be induced on the bottom metal film. At 0.507 THz, the upper surface of the structure induces two opposite loop currents in the presence of electromagnetic waves, and the resulting magnetic moments are equal in size

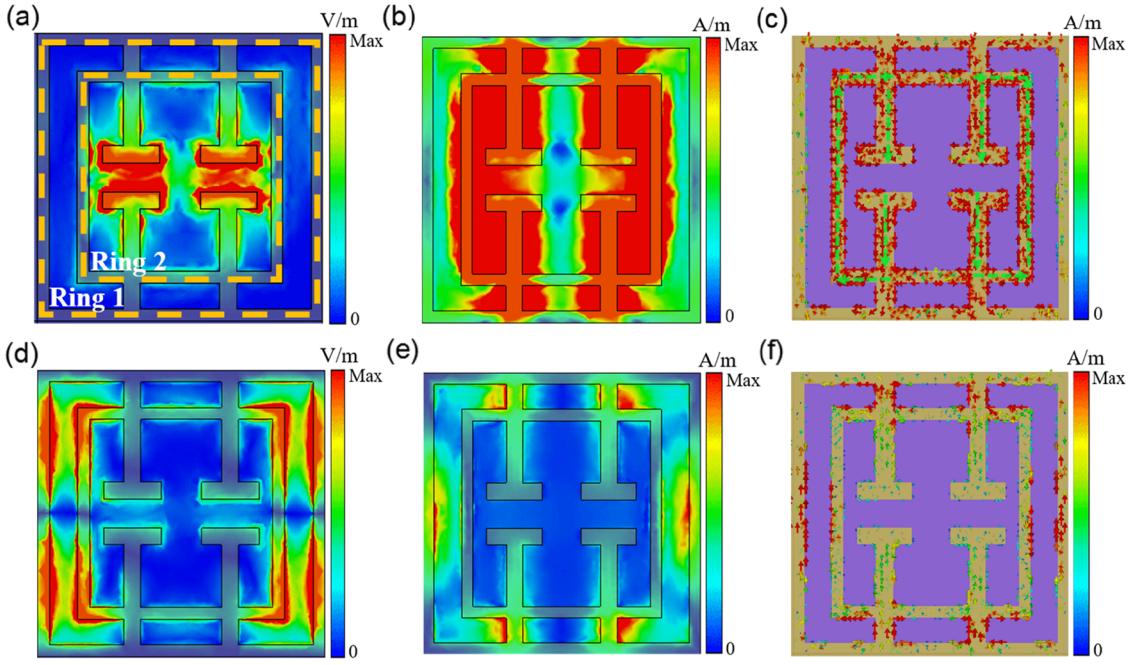

Figure 6. Surface electric field intensity, current density, and magnetic field intensity distribution of the metasurface absorber at different frequencies: (a) surface electric field intensity distribution at 0.507 THz; (b) surface magnetic field intensity distribution at 0.507 THz; (c) surface current distribution at 0.507 THz; (d) surface electric field intensity distribution at 1.101 THz; (e) surface magnetic field intensity distribution at 1.101 THz; (f) surface current distribution at 1.101 THz.

https://doi.org/10.1021/acsomega.2c05016
ACS Omega 2022, 7, 36712−36727

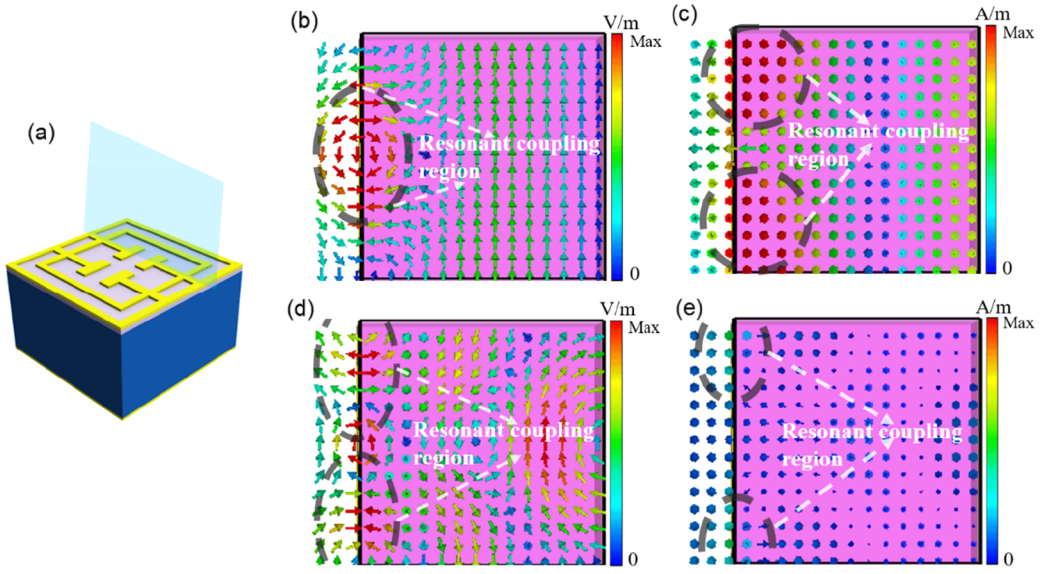

Figure 7. Internal electric field and magnetic field intensity distributions of the metasurface absorber at different frequencies: (a) longitudinal section at the split ring; (b) distribution of electric field intensity at 0.507 THz; (c) distribution of magnetic field intensity at 0.507 THz; (d) distribution of electric field intensity at 1.101 THz; (e) distribution of magnetic field intensity at 1.101 THz.

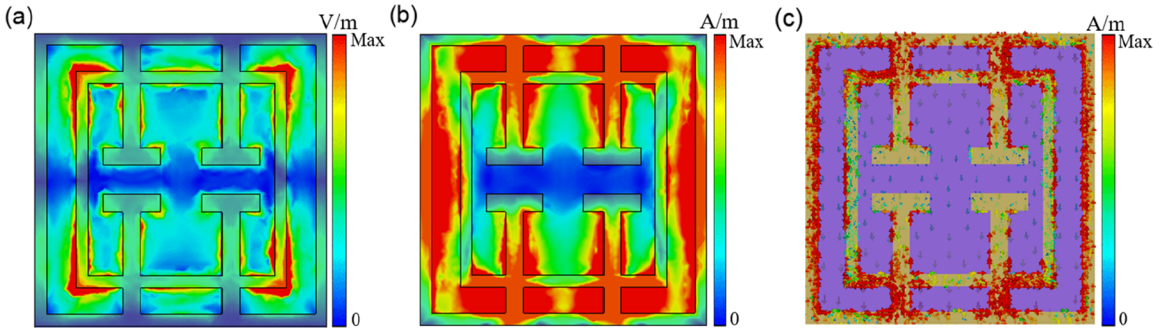

Figure 8. Surface electric field intensity (a), magnetic field intensity (b), and surface current (c) of the metasurface absorber at 0.836 THz.

and opposite in direction. As the magnetic moments cancel each other, a low-radiation RLC resonant mode is thus formed, which helps to enhance the structure's absorption of terahertz radiation. In Figure 6f, at 1.101 THz, the surface current is mainly distributed on the outermost metal ring (Ring 1), the induced charge accumulation on the upper surface is less than 0.507 THz, and the resulting electromagnetic dipole resonance coupling is weak; that is, the absorption peak at 0.507 THz is higher than 1.101 THz. To further reveal the magnetic dipole resonance absorption mechanism of the metasurface absorber, the magnetic field intensity distributions of the absorber at 0.507 and 1.101 THz are shown in Figure 6b,e. At 0.507 THz, the distribution of the magnetic field intensity on the upper surface of the absorber that the magnetic dipole resonance mainly existed in the interior of Ring 1 in the unit structure. Therefore, this electromagnetic resonance effect inside the unit structure can correspond to the fundamental mode of electromagnetic dipole resonance absorption (fundamental mode of resonance absorption, FRA). At 1.101 THz, the magnetic dipole resonance mainly existed between adjacent unit structures, which belongs to electromagnetic dipole resonance coupling absorption between adjacent units (super-model of resonance absorption, SRA). Figure 7 shows the resonance absorption of the electromagnetic dipole inside the medium at 0.507 and 1.101 THz of the metasurface absorber simulated to reveal the electromagnetic dipole resonance absorption mechanism. Figure 7a shows the electromagnetic field distribution on the longitudinal section at the split ring in the absorber. Figure 7b,c shows that the electromagnetic dipole resonance absorption region at 0.507 THz is mainly distributed inside the unit structure, which further proves that it belongs to FRA. At 1.101 THz, the electromagnetic dipole resonance absorption region mainly existed between adjacent unit structures, which also indicates that it belongs to SRA (see Figure 7d,e). Therefore, the metasurface absorber had different absorption modes at different absorption peaks. In addition, at 0.507 THz, the direction of the electric field on the upper surface is basically opposite to the direction of the induced electric field on the lower surface, indicating that the cause of resonant absorption is the electromagnetic dipole resonance formed on the upper and lower surfaces, see Figure 7b.

The above analysis shows different frequency selectivity at 0.507 and 1.101 THz, mainly due to the resonant absorption mode. Although the absorption at 0.507 THz is higher than that at 1.101 THz, the Q-factor at 0.507 THz is smaller than that at 1.101 THz, indicating that the frequency selectivity caused by the SRA is stronger than that of the FRA.

It can also be seen from Table 1 that the *Q*-factor at 0.836 THz (Δf = 0.005, Q = 167.20) has the highest, indicating the best frequency selectivity. The following analysis of the

https://doi.org/10.1021/acsomega.2c05016
ACS Omega 2022, 7, 36712−36727

frequency selectivity characteristics at this frequency point is presented. At 0.836 THz, the electric and magnetic fields not only are distributed in the middle region of the metal Rings 1 and 2 but also have field distribution outside the metal Ring 1 (see Figure 8a,b). This phenomenon shows that at 0.836 THz, the magnetic field energy is mainly distributed inside the unit structure and the region between adjacent unit structures. It can also be seen that the current on the upper surface due to electromagnetic resonance at 0.836 THz is distributed inside the unit structure as well as in the adjacent structural units (see Figure 8c). It is shown that the frequency selectivity characteristics generated at 0.836 THz are produced by the combined effect of FRA and SRA. This also explains the specific reason for the strong frequency selectivity at 0.836 THz.

The above analysis shows that due to electromagnetic induction, the surface metal structure and the underlying metal film have an inverse parallel surface current and charge distribution, forming an electromagnetic dipole inside the device. Through the combined action of the magnetic dipole resonance and the electric dipole resonance, an absorption peak can be generated at a specific frequency, and the perfect absorption of the THz wave can be realized.[26] In addition, the metasurface THz absorption devices have different resonance absorption modes at different frequency points, leading to different frequency selectivities. The metasurface THz absorption devices with strong frequency selectivity can be developed by designing structures with both FRA and SRA. Thus, our work provides a way and theoretical support to realize metasurface THz absorbers with strong frequency selectivity, promising breakthroughs in fields such as sensing and selective thermal imaging.

4. INFLUENCE OF STRUCTURAL PARAMETERS

4.1. Polarization Analysis. Starting with the two incident cases of TE wave and TM wave (the electric field of the electromagnetic wave is parallel to the opening, parallel polarized wave), the polarization characteristics of the structure were analyzed. The absorption of incident electromagnetic waves with the TM mode by the metasurface absorber is shown in Figure 9. Compared with the TE mode

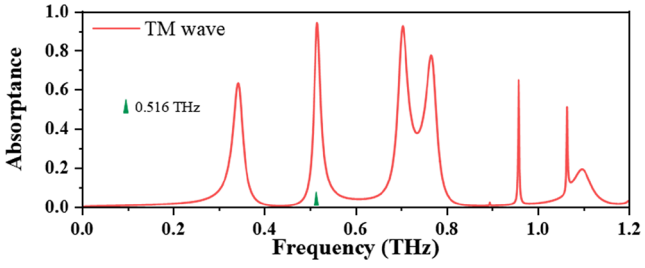

Figure 9. Electromagnetic wave absorption spectrum of the metasurface absorber (TM mode) at 0−1.2 THz.

(see Figure 4), in the TM mode, $A(f_0 = 0.516\ \text{THz})$ was only 94%, and the absorption effect was not significant at other absorption peak positions, so the structure was a polarization sensitive structure.

4.2. Incidence Angle Analysis. In most cases, electromagnetic waves are not perpendicularly incident and usually have a certain angle with the metasurface. Therefore, it is necessary to study the influence of different modes of electromagnetic waves obliquely incident on the metasurface absorber on its absorption performance (see Figure 10). Figure 11a,b shows the absorption spectra in the TE wave and the TM wave mode when the incident angle (θ) of the electromagnetic wave is 0−80°. As shown in Figure 11a, the absorption spectrum of the absorber was basically the same in the range of θ = 0−40°, with good incident angle compatibility. When θ = 0−80°, the original absorption peak position moved to the high frequency; that is, the absorption peak blue-shifted. When θ = 60°, $A(f_0 = 0.374\ \text{THz}) = 99.67$ and $A(f_0 = 0.513\ \text{THz}) = 90.14\%$, indicating that the designed metasurface absorber had good incident angle compatibility. With the change of θ, not only did the absorption peaks move but also new absorption peaks appeared. For example, when θ = 20°, a new absorption peak appeared at 1.146 THz, and $A(f_0 = 1.146\ \text{THz}) = 48.37\%$; the absorption peak was generated by gradual impedance matching. When θ = 80°, the absorption peak appeared to be greatly attenuated; the reason is that when the metasurface absorber responded to external electromagnetic waves, electrical resonance was relatively easy to achieve, while magnetic resonance was relatively difficult and its resonance intensity was weak. For the TE mode incident electromagnetic wave, as θ increased, the component of the magnetic field H in the y-direction ($|H_y|$) became increasingly smaller, and eventually, it was difficult to provide enough flux to maintain a certain magnetic resonance; therefore, the magnetic resonance did not match the electrical resonance, causing a mismatch in the impedance of the metasurface absorber, and it was difficult to maintain a high absorptance (see Figure 11a). For the TM mode incident electromagnetic wave, the magnetic field was always along the y-direction, so the response of the metasurface to the magnetic field remained constant, and a strong magnetic resonance could be achieved at different θ, which could maintain a high absorptance (see Figure 11b). The absorption peak of the incident electromagnetic wave at a single frequency point in the TM wave mode was lower than that in the TE wave mode because it was easier for the designed metasurface structure to achieve impedance matching, with a stronger coupling effect on the TE wave.[19,22,24] In addition, the phenomenon of variance in the absorption spectrum with θ can also be explained by interference theory:[30−32] the electromagnetic waves incident at different angles are reflected and transmitted multiple times on the interface of the metasurface and, finally, superimposed multiple times in the incident surface. As the incident angle increased, interference cancellation occurred after passing through the metasurface, so the absorptance at the absorption peak became smaller. Similarly, the newly emerged absorption peaks had higher absorptances due to enhanced coherence.

4.3. Analysis of Opening Size. By adjusting the size of the opening L_6 from 10 to 14 μm, the change in the absorption performance of the metasurface absorber was observed (see Figure 12). The unit structure of the metasurface absorber can be equivalent to the RLC oscillator circuit[33] (see Figure 12a). The RLC oscillator circuit was in the parallel mode; $C = C_1 + C_2$; $\frac{1}{L} = \frac{1}{L_1} + \frac{1}{L_2}$; $\frac{1}{Z_{\text{Device}}} = \frac{1}{Z_1} + \frac{1}{Z_2}$; the capacitance, inductance, and impedance of the SiO_2 and Si dielectric layers have not changed; and this part of the influence can be ignored. Its equivalent impedance (Z_{Device}) and phase difference (ϕ) can be expressed as

https://doi.org/10.1021/acsomega.2c05016
ACS Omega 2022, 7, 36712−36727

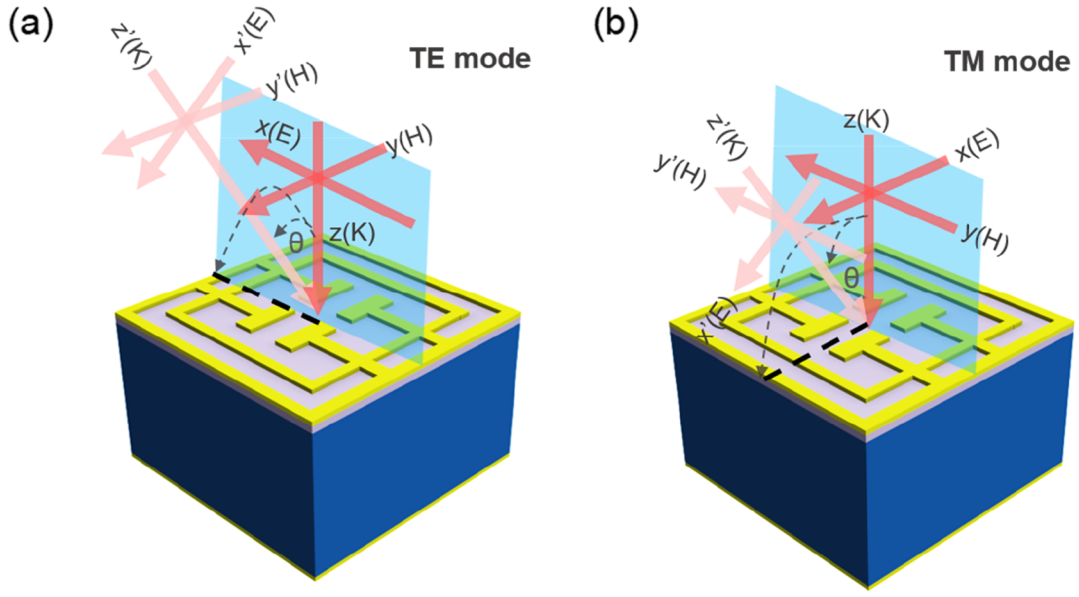

Figure 10. (a) Schematic diagram of incident THz waves in different modes: (a) TE mode and (b) TM mode.

$$Z_{\text{Device}} = \sqrt{\frac{R^2 + (\omega \text{L})^2}{(1 - \omega^2 \text{LC})^2 + (\omega \text{CR})^2}} \tag{12}$$

$$\phi = \arctan\frac{\omega \text{L} - \omega \text{C}[R^2 + (\omega \text{L})^2]}{R} \tag{13}$$

When the polarization electric field direction of the incident electromagnetic wave was parallel to the split ring composite structure, a relatively obvious resonance peak appeared at a specific frequency, and according to eq 12, the frequency at the resonance peak f_0 ($f_0 = \omega_0/2\pi, \phi = 0$) can, thus, be expressed as[29]

$$\omega \text{L} - \omega \text{C}[R^2 + (\omega \text{L})^2] = 0 \tag{14}$$

$$\omega = \omega_0 = \sqrt{\frac{1}{\text{LC}} - \left(\frac{R}{L}\right)^2} \tag{15}$$

$$f_0 = \frac{1}{2\pi}\sqrt{\frac{1}{\text{LC}} - \frac{R^2}{L^2}} \tag{16}$$

Since the electrical conductivity of the metasurface metal material was relatively large, the internal resistance value R of the metal metasurface could be ignored, and, as a result, eq 16 can be simplified to eq 17[34,35]

$$f_0 = 1/(2\pi\sqrt{\text{LC}}) \tag{17}$$

$$C = \frac{\varepsilon_0 S}{D} \tag{18}$$

With the increase of P_6 (D increases), C decreases and L also decreases, and so f_0 increases; that is, the absorption peak exhibits a blue shift. In Figure 12c, the position of the absorption peak at 0.507 THz appeared blue-shifted with the increase of P_6. However, the position of the absorption peak at 0.836 THz changed little and remained almost unchanged, and there was no obvious blue shift (see Figure 12d). For electromagnetic dipole resonance, the RLC circuit can effectively analyze and predict resonance absorption frequency. In Figure 6a,e, at 0.507 THz, the electric and magnetic fields were mainly distributed in the middle region of the unit structure, the fundamental electromagnetic dipole resonance of the unit structure. According to the RLC circuit model, on one hand, due to the resonance of the electromagnetic dipole, with the increase of the opening size, the equivalent capacitance C decreases, and the absorption peak moves to a high frequency. On the other hand, due to the supermodel resonance between adjacent unit structures, increasing the inductance (L increases), the peak frequency shifts to a low frequency,[36] with an overall result being an absorption peak position basically maintained around 0.836 THz.

5. TUNABLE METASURFACE THZ ABSORBER

For the metasurface absorber previously described, modulation of the absorption frequency and absorption intensity of the absorber can only be achieved by changing the structural parameters of the metasurface. However, this modulation method has disadvantages, such as inconvenience and high cost in practical applications. Artificial metasurfaces usually consist of sub-wavelength metallic resonant cells, and the resonant frequency ($f \propto 1/\sqrt{\text{LC}}$) of the cell structure can be described by the LC equivalent circuit model. Therefore, the resonant frequency of the cell structure can be changed if the inductance or capacitance can be changed by an external signal.[37,38] In this section, the modulation of the metasurface absorber is realized by applying different bias voltages to the 2D materials in the metasurface and irradiating the photosensitive semiconductor silicon (SI-ps) with different illuminances (E_L). Simulation experiments showed that under certain bias voltage or illumination conditions, the designed tunable metasurface absorber had an evident modulation effect at a specific frequency point.

5.1. Based on 2D Materials. Graphene currently has a great applicational value in the fields of electronics, optics, and materials science. It has remarkable properties, such as optical transparency, flexibility, and high electron mobility in the THz band. In addition, graphene has a gapless band structure, and the surface conductivity can be adjusted by chemical doping and applying bias voltage.[39−44] When electromagnetic waves are incident on the graphene surface, a strong surface plasmon

https://doi.org/10.1021/acsomega.2c05016
ACS Omega 2022, 7, 36712−36727

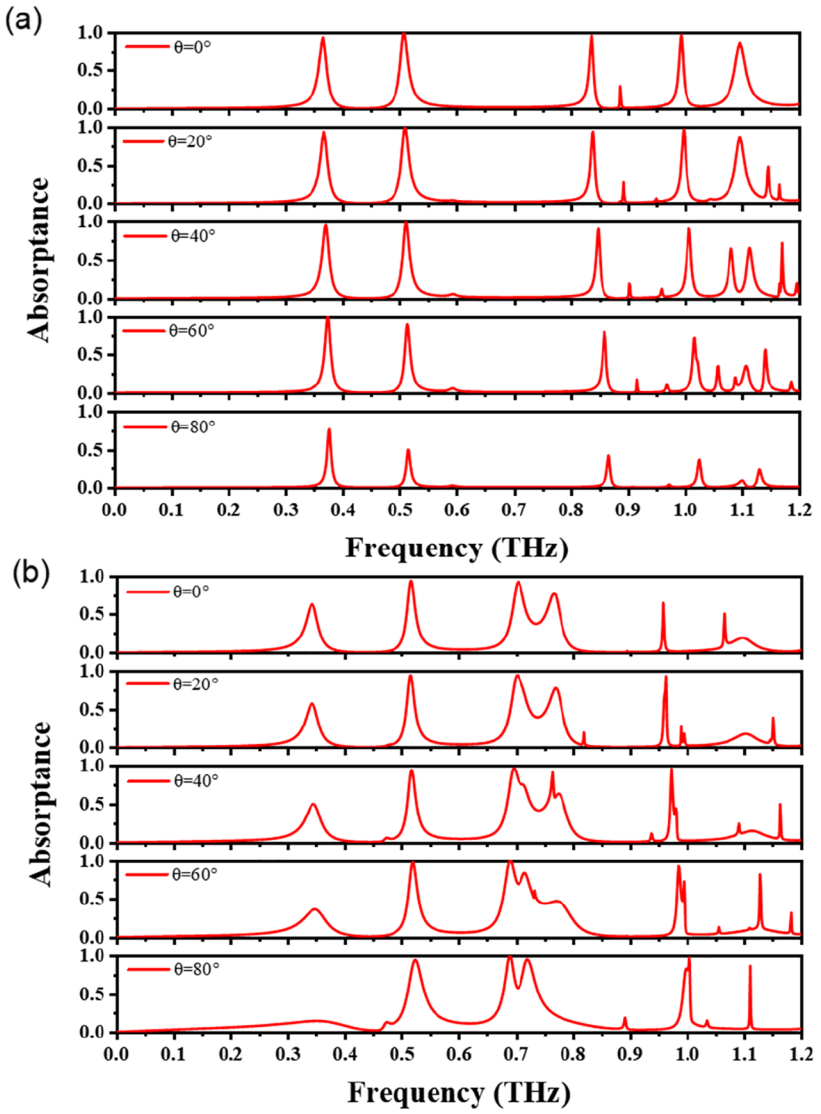

Figure 11. (a) Absorption spectra of the metasurface absorber under different incident angles of electromagnetic waves in the TE mode and (b) TM mode.

resonance is excited, resulting in strong electromagnetic energy and low propagation loss. Therefore, graphene has received great attention due to its applications in THz devices, such as modulators, absorbers, filters, detectors, and polarizers. The graphene surface conductivity (σ_g) can be calculated by the Kubo formula[45−48]

$$\sigma_g = \frac{ie^2(\omega - i\Gamma)}{\pi\hbar^2} \times \left[\frac{1}{(\omega - i\Gamma)^2} \int_0^\infty \left(\frac{\partial f_d(\varepsilon)}{\partial \varepsilon} - \frac{\partial f_d(-\varepsilon)}{\partial \varepsilon} \right) \varepsilon d\varepsilon - \int_0^\infty \frac{f_d(-\varepsilon) - f_d(\varepsilon)}{(\omega - i\Gamma)^2 - 4(\varepsilon/\hbar)^2} d\varepsilon \right] \quad (19)$$

where $e = 1.602 \times 10^{-19}$ C is the electron charge, ω is the angular frequency, $\hbar = h/2\pi = 1.054 \times 10^{-34}$ J·s is the reduced Planck constant, $T = 300$ K is the temperature, ε is the kinetic energy of the electron (hole), $f_d(\varepsilon) = (e^{(\varepsilon-\mu_c)/(k_B T)} + 1)^{-1}$ is the Fermi Dirac distribution, $k_B = 1.38 \times 10^{-23}$ J/K is the Boltzmann constant, μ_c is the chemical potential ($T = 300$ K, $\mu_c \approx E_f$, E_f the Fermi level), and Γ is the collision frequency. When $k_B T < |\mu_c|$, eq 19 can be approximately expressed as

$$\sigma_g = \sigma_{g-\text{intra}} + \sigma_{g-\text{inter}} \quad (20)$$

where $\sigma_{g\text{-intra}}$ is the intraband conductivity and $\sigma_{g\text{-inter}}$ is the interband conductivity; they can be represented by eqs 21 and 22, respectively

$$\sigma_{g-\text{intra}} = i\frac{e^2 k_B T}{\pi\hbar^2(\omega - i\Gamma)} \left[\frac{\mu_c}{k_B T} + 2\ln(e^{-\mu_c/k_B T} + 1) \right] \quad (21)$$

$$\sigma_{g-\text{inter}} = \frac{ie^2}{4\pi\hbar} \ln \left[\frac{2|\mu_c| - (\omega - i\Gamma)\hbar}{2|\mu_c| + (\omega - i\Gamma)\hbar} \right] \quad (22)$$

In the low-frequency range, $\hbar\omega \ll 2|\mu_c|$; that is, the photon energy is much smaller than the E_f, and the interband jump is forbidden according to the Pauli blocking principle, so $\sigma_{g\text{-inter}}$ is negligible and its total conductivity is dominated by $\sigma_{g\text{-intra}}$.[49]

https://doi.org/10.1021/acsomega.2c05016
ACS Omega 2022, 7, 36712−36727

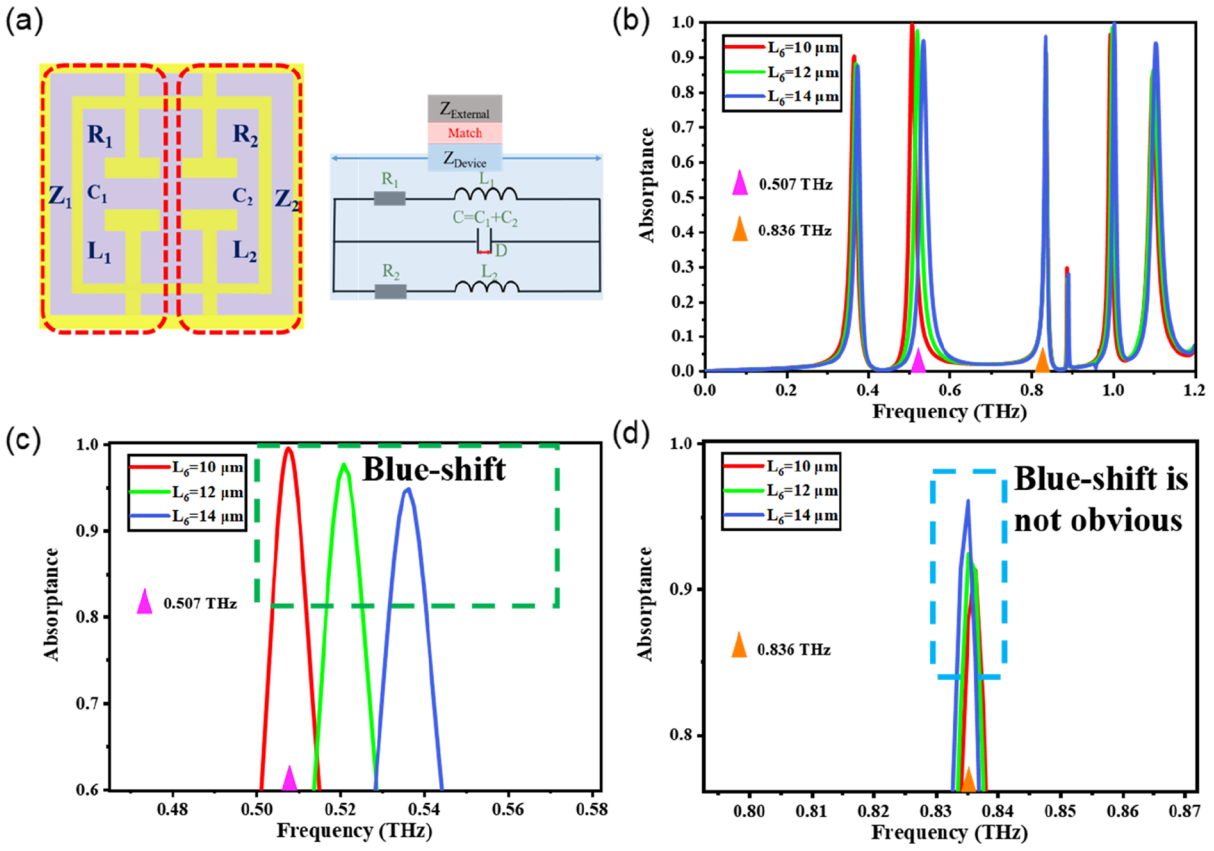

Figure 12. Metasurface absorber performance with different opening sizes: (a) equivalent RLC oscillator circuit; R is the equivalent resistance, L is the equivalent inductance of the split-ring composite structure, C is the equivalent capacitance of the split-ring composite structure, $\varepsilon_0 = 8.85 \times 10^{-12}$ $C^2/(N{\cdot}m^2)$ is the vacuum dielectric constant, D is the distance between the equivalent plate capacitors, S is the area of equivalent parallel plate capacitor, $Z_{External}$ (Z_0) is the external impedance, and Z_{Device} (Z_L) is the equivalent impedance; (b) absorption spectrum; (c) peak absorption around 0.507 THz, and the absorption peak appears blue-shifted; (d) peak absorption around 0.836 THz, and the position of the absorption peak remains basically unchanged.

Therefore, the σ_g can be directly expressed by eq 20. When $\mu_c \gg k_B T$, the σ_g is approximately linearly related to it[50]

$$\sigma_g \approx \frac{ie^2\mu_c}{\pi\hbar^2(\omega - i\Gamma)} \approx \frac{ie^2E_f}{\pi\hbar^2(\omega - i\Gamma)} \tag{23}$$

From eq 23, it can be seen that σ_g is related to μ_c and ω, so μ_c can be controlled by adjusting the applied voltage or by chemical doping to tune the absorption frequency. Figure 13a shows a schematic diagram of the structure of the absorber regulated E_f by the gate voltage and the corresponding absorption spectra at different E_f. The thickness of graphene is 0.3 μm, and when E_f = 0−0.08 eV, the absorption spectra results are obtained as shown in Figure 13b,c. As can be seen, the absorption spectrum changes significantly at 0.967 THz with the increase of E_f. As E_f increases, the carrier density also increases, and the resonance amplitude gradually increases, which also shows that the resonance absorption of the absorber can be tuned by changing E_f. The main reason for these results is that with the change of E_f, σ_g changes accordingly and results in a good match between the impedance of the absorber and the impedance of the free space.

To further study the tunable performance of the metasurface absorber, the expression for the MD of the absorptance is as follows[51]

$$\mathrm{MD} = \frac{A_{MAX} - A_{MIN}}{A_{MAX}} \tag{24}$$

where A_{MAX} and A_{MIN} are the maximum and minimum absorptances of metasurfaces at different σ_g, respectively. From Figure 13c, the MD is 26% at 0.42 THz and 62.17% at 0.967 THz, which has a significant tunability of the absorption spectrum amplitude. In addition, there is no significant red shift or blue shift of the absorption peaks under bias modulation.

The graphene-based THz metasurface modulator designed in this section achieves an MD of more than 62.17% at a specific frequency point, and graphene has a high electron mobility of up to 2×10^5 cm^2V^{-1} s^{-1} (suspended graphene), which enables a high modulation rate (MR). The MR of graphene-based THz metasurface modulation devices is investigated in the literature within KHz−MHz[52−55] or even faster. We compared the performance of different types of metasurface THz modulators under electrical modulation, as shown in Table 2.

First of all, it can be seen from Table 2 that the overall performance of the metasurface THz modulator designed in this section has a great advantage in terms of MD as well as MR compared to other types of modulators. Although the temperature-controlled VO_2-based metasurface THz modulator has a relatively large MD, the temperature-dependent properties exhibited by the VO_2 material make the MR of the

https://doi.org/10.1021/acsomega.2c05016
ACS Omega 2022, 7, 36712−36727

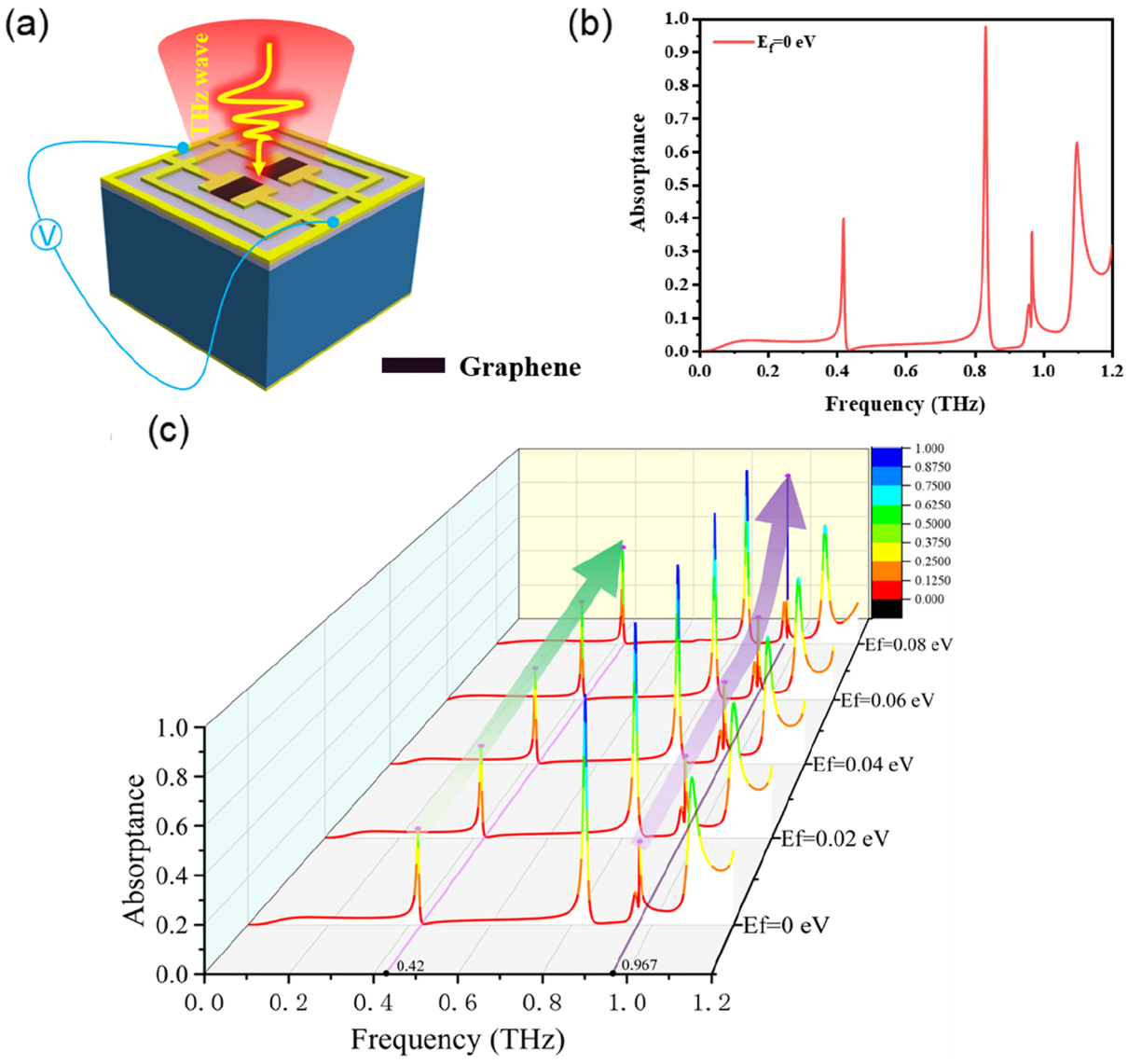

Figure 13. (a) Schematic diagram of the structure of a switchable metasurface THz absorber based on graphene; (b) absorptance spectrum without gate voltage; (c) absorption spectrum of E_f = 0−0.08 eV.

Table 2. Different Types of THz Metasurface Modulators under Electrical Modulation

materials (structures)	modulation band (THz)	MD_{Max} (%)	MR_{Max}	refs.
graphene	0−1.2	62.17	≈ KHz-MHz	our work
graphene	0−2	47		56
graphene	0.4−1.5	22		57
graphene	2.2−3.1	18		53
graphene	0.57−0.63	16		54
MEMS	0.55−0.8	50	≈ KHz-MHz	11,58,59
VO_2 (thermal control)	0.3−1.5	65	≈ ms	60,61
n-GaAs	0.2−2	33	KHz	62
n-GaAs	0.25−2.25	50	KHz	63
GaAs-HEMT	0.1−1.1	<33	≈ MHz	64
GaN-HEMT	0.2−0.7	85	≈ GHz	65,66

device slower and thus have a time constant of tens of milliseconds or even longer, which is not suitable for application in THz high-speed communication systems. Although the GaAs high-electron mobility transistor (HEMT)-based THz metasurface modulator achieves an MR of MHz, the MD is not ideal, and the process is complex and costly. The GaN-HEMT-based THz metasurface modulator achieves 85% MD, but the MR is maintained at GHz, which is more difficult to achieve higher MR and also has the problems of a complex process and high cost. The microelectromechanical system (MEMS)-based metasurface THz modulation devices can achieve higher MRs, but the adjustment is relatively cumbersome and not precise enough. Graphene has high electron mobility at room temperature, high thermal conductivity, unique optical properties, and mechanical properties that make it possible to realize THz modulation devices with a high MR and a large MD at the same time. The graphene-based double open-loop metasurface THz modulation device designed in this section has excellent MR and MD at the same time, which provides an important research idea for the development of metasurface THz devices with high integration.

5.2. Based on Photosensitive Semiconductor Silicon. In this section, a 0.3 μm thick SI-ps is placed at the split ring to

https://doi.org/10.1021/acsomega.2c05016
ACS Omega 2022, 7, 36712−36727

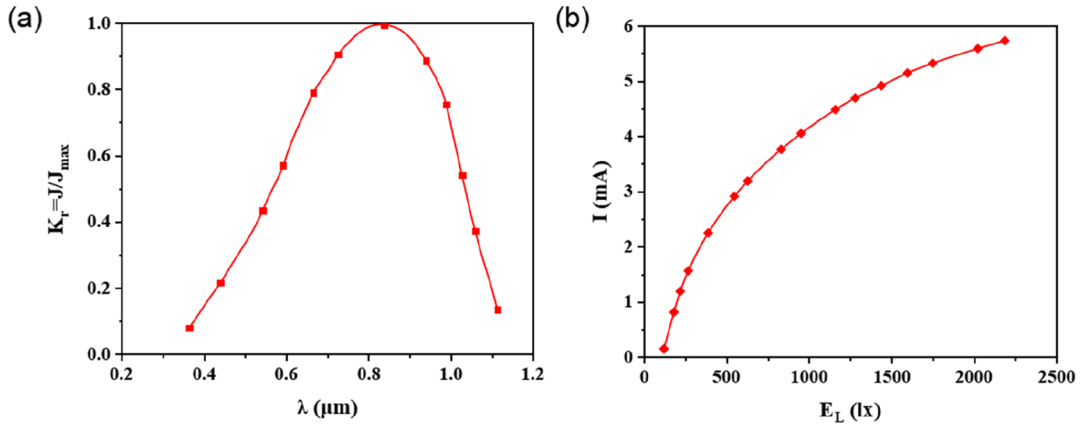

Figure 14. Characteristics of photosensitive semiconductor silicon: (a) spectral characteristics and (b) illumination characteristics.

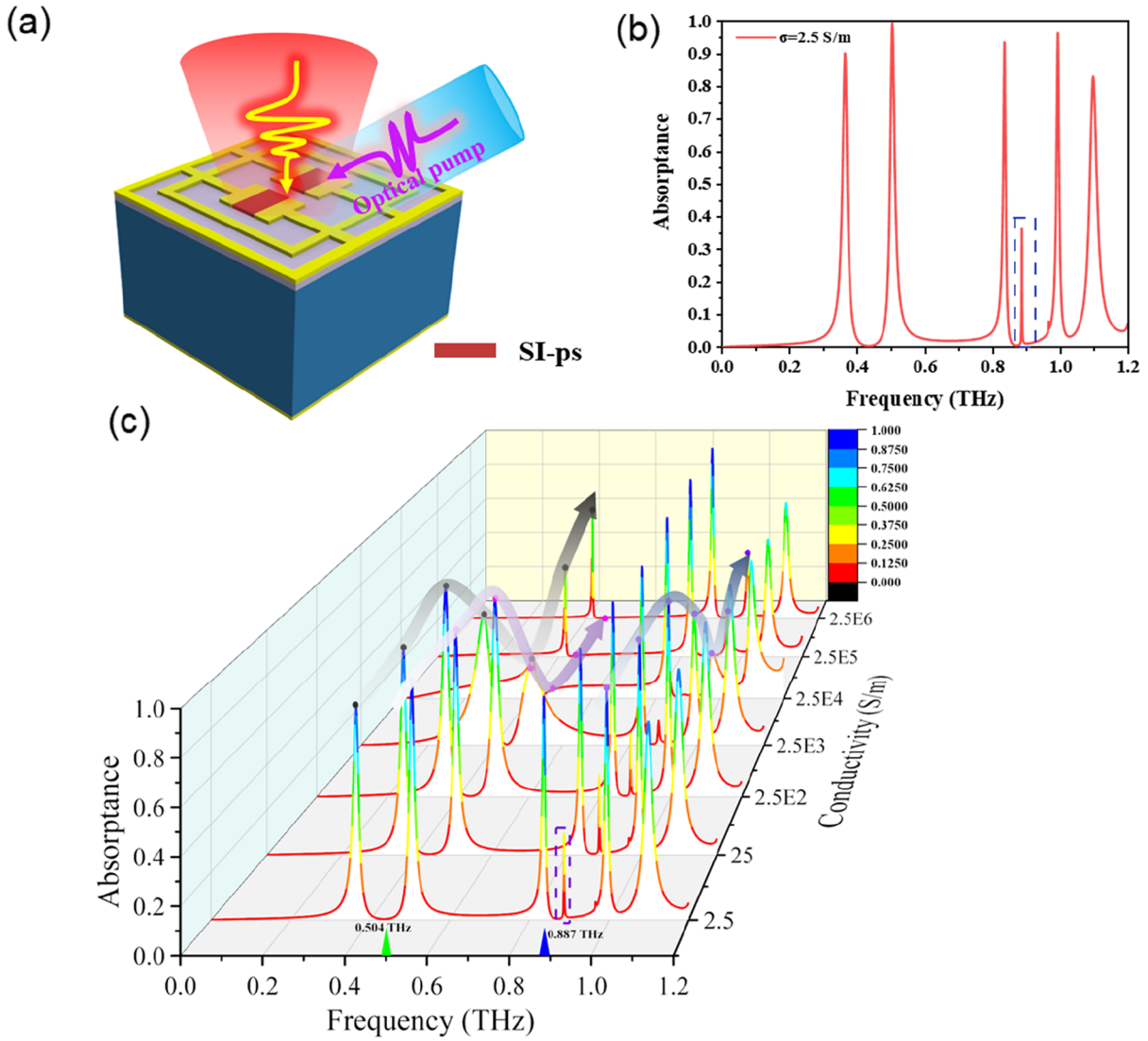

Figure 15. (a) Schematic diagram of the metasurface THz structure with a photosensitive semiconductor silicon structure; (b) absorption spectrum when $\sigma_{SI\text{-}ps}$ = 2.5 S/m; (c) absorption spectra of semiconductor silicon at different conductivities.

examine the realization of a metasurface absorber with tunable properties by different E_L. When the voltage across the optoelectronic device is certain, the output photocurrent I (photocurrent density, J) varies with the wavelength for the same incident power[67,68] if monochromatic light of a certain wavelength is irradiated on the optoelectronic device. The relative sensitivity (K_r) of SI-ps is generally expressed as a percentage of the photocurrent and the maximum photocurrent (I_{max}), that is, $K_r = \frac{I}{I_{max}} = \frac{J}{J_{max}}$. Figure 14a shows the

https://doi.org/10.1021/acsomega.2c05016
ACS Omega 2022, 7, 36712−36727

Table 3. Shifts in Absorption Peak Positions of Metasurface Absorbers under Different Photoexcited Intensities

photosensitive semiconductor material	initial position of absorption peak (σ = 2.5 S/m)	absorption peak position (σ = 2.5 × 10^5 S/m)	absorption peak position (σ = 2.5 × 10^6 S/m)
Si	0.364 THz	0.420 THz	0.420 THz
Si	0.504 THz	disappear	disappear
Si	0.835 THz	0.833 THz	0.833 THz
Si	0.887 THz	disappear	disappear
Si	0.993 THz	0.956 THz	0.956 THz
Si	1.098 THz	1.090 THz	1.090 THz

optimal sensitivity using near-infrared light at a wavelength of around 840 nm. When the photovoltaic device voltage is certain, illumination characteristics exist on the I and E_L of the photoresistor, that is, $E_L \propto I$ (see Figure 14b). According to the formula[29]

$$J = \sigma_{SI-ps} E \tag{25}$$

$E_L \propto I$ (or J) $\propto \sigma_{SI\text{-}ps}$, the current density ($J$) is proportional to the electrical conductivity of the photosensitive semiconductor silicon ($\sigma_{SI\text{-}ps}$), and $\mathbf{E}$ is the electric field intensity. As E_L increases, the carrier concentration in SI-ps continues to increase, $\sigma_{SI\text{-}ps}$ increases, and SI-ps gradually changes from a semiconductor state to a conductor state, which in turn affects the resonant frequency of the metasurface.

Figure 15b shows the metasurface absorption spectrum of $\sigma_{SI\text{-}ps}$ = 2.5 S/m, and Figure 15c shows the absorption spectrum of the metasurface absorber of SI-ps under photoexcited modulation; the $\sigma_{SI\text{-}ps}$increases from 2.5 S/m to 2.5 × 10^6 S/m under photoexcited modulation. When $\sigma_{SI\text{-}ps}$ = 2.5 S/m (without external photoexcitation), a total of 6 absorption peaks appear. At 0.364, 0.504, 0.835, and 0.993 THz, $A(f_0) > 90\%$, and $A(f_0 = 0.504\ \text{THz}) > 99.5\%$. At 0.887 THz (blue dashed box), where the absorption peak is minimum, $A(f_0) \approx 36.3\%$. When $\sigma_{SI\text{-}ps}$ = 2.5 S/m, $A(f_0 = 0.364\ \text{THz}) \approx 90.1\%$. With an increase in photoexcited intensity, $\sigma_{SI\text{-}ps}$ = 2.5 × 10^5 S/m, $A(f_0 = 0.42\ \text{THz}) \approx 48.96\%$, and the absorption peak shifts to blue from 0.364 THz to 0.42 THz, resulting in a 56 GHz shift. Table 3 lists the shifts of the absorption peaks at the six absorption peaks of the tunable metasurface absorber with the change of illumination intensity. When $\sigma_{SI\text{-}ps}$ = 2.5 × 10^6 S/m, only four corresponding absorption peaks appear; the absorption peaks $\sigma_{SI\text{-}ps}$ = 2.5 S/m at 0.504 and 0.887 THz disappear, indicating that this structure produces a solid waveform modulation effect. As $\sigma_{SI\text{-}ps}$ increases to 2.5 × 10^5 S/m, the absorption peaks at 0.835, 0.993, and 1.098 THz shift to a red state. When $\sigma_{SI\text{-}ps}$ increases from 2.5 × 10^5 to 2.5 × 10^6 S/m, the position of the absorption peak remains unchanged because when the photoexcited energy is strong, the silicon overflows from a semiconductor to a conductor; in other words, capacitive conduction and the charge can pass smoothly through the semiconductor material, resulting in a relatively stable state of the absorption peak position. Little difference exists within the absorption spectra when $\sigma_{SI\text{-}ps}$ = 2.5 and 25 S/m; the main concurrent reasons are that the $\sigma_{SI\text{-}ps}$ does not change significantly, the conductivity is not significantly enhanced, and the impact on the metasurface resonance frequency is small. The modulation effect on the metasurface absorber becomes apparent as $\sigma_{SI\text{-}ps}$ continues to increase. When $\sigma_{SI\text{-}ps}$ is 2.5 × 10^3 and 2.5 × 10^4 S/m, the absorption spectra of the metasurface absorber fluctuate greatly. However, when $\sigma_{SI\text{-}ps}$ is 2.5 × 10^5 and 2.5 × 10^6 S/m, the absorption spectra of the metasurface absorber tend to be stable with little change. The main reason for this is that when the photoexcited energy is very strong, the silicon transitions from the semiconductor to the conductor, and the charge can pass through the semiconductor material smoothly, resulting in a relatively stable position of the absorption peak, as shown in the three colored trend lines in Figure 15c. The colored trend line corresponds to the changing trend of the absorption peak of the metasurface absorber at $\sigma_{SI\text{-}ps}$ = 2.5 S/m:

I At 0.364 THz, when $\sigma_{SI\text{-}ps}$ = 2.5 S/m, $A(f_0) \approx 90.1\%$; when $\sigma_{SI\text{-}ps}$ = 2.5 × 10^4 S/m, $A(f_0) \approx 21\%$ and the MD = 76.69%; when $\sigma_{SI\text{-}ps}$ = 2.5 × 10^6 S/m, $A(f_0) \approx 61.86\%$ and the MD = 31.4%.

II At 0.504 THz, when $\sigma_{SI\text{-}ps}$ = 2.5 S/m, $A(f_0) \approx 99.5\%$; when $\sigma_{SI\text{-}ps}$ = 2.5 × 10^4 S/m, $A(f_0) \approx 4.7\%$ and the MD = 95.28%. When $\sigma_{SI\text{-}ps}$ = 2.5 × 10^6 S/m, $A(f_0) \approx 0.6\%$ (the absorption peak corresponding to $\sigma_{SI\text{-}ps}$ = 2.5 S/m disappears) and the MD > 99.99% (≈100%). Similarly, at 0.887 THz, the MD of absorptance can also reach ≈100%.

III At 0.993 THz, when $\sigma_{SI\text{-}ps}$ = 2.5 S/m, $A(f_0) \approx 96.5\%$; when $\sigma_{SI\text{-}ps}$ = 2.5 × 10^4 S/m, $A(f_0) \approx 24.3\%$ and the MD = 74.82%; when $\sigma_{SI\text{-}ps}$ = 2.5 × 10^6 S/m, $A(f_0) \approx 37.6\%$ and the MD = 61%.

The double open-loop THz metasurface modulation device based on SI-ps designed in this section achieves 100% MD at a specific frequency point under optical pumping conditions. In addition, the modulator has distinct multi-stage modulation characteristics under different optical pumping conditions, which enable multi-stage modulation of THz signals. The different types of metasurface THz modulators under optical pumping conditions are described below and are shown in Table 4. From Table 4, the MD of our designed THz modulation device is better than that of other devices. Our device has a simple structure and is easy to precisely modulate

Table 4. Different Types of THz Metasurface Modulators under Optical Modulation

materials (structures)	modulation band (THz)	MR_{MAX}(%)	refs.
Si	0−1.2	≈100	our work
Si	0.25−2	38	69
GaAs	0−2	70	70
graphene/Ge	0.25−1	94	71
graphene/Ge	0.2−1.4	62	72
graphene-Si	0.4−2	83	73
liquid crystal	2−6	75	74
one-dimensional photonic crystal	0.3−0.9	50	75
nonlinear photonic crystal	1−1.012	20.3 dB	76

https://doi.org/10.1021/acsomega.2c05016
ACS Omega 2022, 7, 36712−36727

compared to graphene-based germanium substrate modulation devices. Because germanium (Ge) has a short carrier lifetime and is influenced by temperature, it is not conducive to precise multi-stage modulation. Although the THz modulation devices based on liquid crystal materials can achieve an MD of 20.3 dB (MD = 99.07%) at a specific frequency point, the liquid crystal materials themselves have some defects and shortcomings, such as being more sensitive to temperature, so the operating environment is somewhat limited. At the same time, the optical response time of liquid crystal modulators is usually only milliseconds, which is much slower compared to semiconductor materials. These characteristics of the limitations of the liquid crystal-based tunable metasurface devices must be applied if the working environment is not harsh and MR requirements are not high devices.

The two designed modulation devices show that the graphene-based metasurface THz modulation device has the advantages of large MD and ultra-fast MR under electrical modulation; the photoexcited metasurface THz absorber achieves a large absorption MD (≈100%) at multiple frequencies with excellent absorption spectrum modulation, which greatly expands the scope and direction of the absorber applications. The tunable terahertz metasurface will be a very interesting research direction. We believe that the hybrid structured tunable terahertz metasurfaces have an important position in the aspect of tunable metasurfaces, and the choice of the active medium plays a key role in their development. The ideal active medium should not only have good tunable optical properties and stability but also be suitable for larger-scale production and processing; for example, graphene as the active medium for the graphene/metal metasurface hybrid structure will occupy an important position in the research of tunable terahertz and optical metamaterials.

Therefore, based on the analysis of the above results, it can be seen that device tunability is achieved by embedding tunable components such as microwave diodes, variable capacitors, controllable materials (graphene, ferrite, ferromagnets, liquid crystal materials, etc.), and MEMS in a periodic structure. Such tunable THz absorbers can be used in beam-steerable antennas, hyperspectral thermal imaging systems, and sensors.

6. CONCLUSIONS

We have designed multiple frequencies of the metasurface THz perfect absorber using a double-squared open ring structure with two different resonant electromagnetic dipoles. Strong absorption 94.50% at 0.366 THz, 99.99% at 0.507 THz, 95.65% at 0.836 THz, 98.80% at 0.996 THz, and 86.70% at 1.101 THz have been realized due to the resonances of FRA and SRA, and the strong frequency selectivity at 0.836 THz (Q-factor = 167.20) and 0.996 THz (Q-factor = 166.00) is attributed to the common effect of FRA and SRA when the electric field direction of the electromagnetic wave is incident perpendicular to the opening. The effect of varied incident angles of polarized electromagnetic waves shows good incidence angle compatibility. We find that for the TM mode, the resonance peak absorption varies only slightly over a large range of incident angles and provides a reasonable explanation for the phenomenon. The equivalent RLC oscillation circuit model reasonably explains the shift of the absorption peak position as the opening sizes of the THz absorber change. Furthermore, by embedding 2D materials and photosensitive semiconductor materials into periodic structural units, a tunable THz metasurface absorber with excellent properties has been realized. Numerical simulations show that MD ≈ 100% has been achieved at 0.504 THz and 0.887 THz by adjusting the $\sigma_{SI\text{-}ps}$, indicating that the device has excellent absorption spectrum tuning capability. Our results provide important theoretical support and research ideas for the development of metasurface THz absorption devices with strong frequency selectivity and excellent absorption spectrum modulation, which will greatly promote the application of metasurface THz absorption devices in resonators, sensing, bio-detection, and selective thermal imaging.

DATA AVAILABILITY

The data that support the findings of this study are available within the article and its Supporting Information

AUTHOR INFORMATION

Corresponding Author

Zhiming Huang − *State Key Laboratory of Infrared Physics, Shanghai Institute of Technical Physics, Chinese Academy of Sciences, Shanghai 200083, P. R. China; Hangzhou Institute for Advanced Study, University of Chinese Academy of Sciences, Hangzhou 310024, P. R. China; Institute of Optoelectronics, Fudan University, Shanghai 200438, P. R. China; University of Chinese Academy of Sciences, Beijing 100049, P. R. China*; Email: zmhuang@mail.sitp.ac.cn

Authors

Qiangguo Zhou − *State Key Laboratory of Infrared Physics, Shanghai Institute of Technical Physics, Chinese Academy of Sciences, Shanghai 200083, P. R. China; University of Chinese Academy of Sciences, Beijing 100049, P. R. China;* orcid.org/0000-0002-3989-6655

Wanli Ma − *State Key Laboratory of Infrared Physics, Shanghai Institute of Technical Physics, Chinese Academy of Sciences, Shanghai 200083, P. R. China; University of Chinese Academy of Sciences, Beijing 100049, P. R. China;* orcid.org/0000-0002-4153-0994

Tuntan Wu − *State Key Laboratory of Infrared Physics, Shanghai Institute of Technical Physics, Chinese Academy of Sciences, Shanghai 200083, P. R. China; Hangzhou Institute for Advanced Study, University of Chinese Academy of Sciences, Hangzhou 310024, P. R. China; University of Chinese Academy of Sciences, Beijing 100049, P. R. China;* orcid.org/0000-0002-7640-4453

Yongzhen Li − *State Key Laboratory of Infrared Physics, Shanghai Institute of Technical Physics, Chinese Academy of Sciences, Shanghai 200083, P. R. China; University of Chinese Academy of Sciences, Beijing 100049, P. R. China*

Qinxi Qiu − *State Key Laboratory of Infrared Physics, Shanghai Institute of Technical Physics, Chinese Academy of Sciences, Shanghai 200083, P. R. China; University of Chinese Academy of Sciences, Beijing 100049, P. R. China;* orcid.org/0000-0002-7044-7911

Jiaxin Duan − *State Key Laboratory of Infrared Physics, Shanghai Institute of Technical Physics, Chinese Academy of Sciences, Shanghai 200083, P. R. China; School of Science, Xihua University, Chengdu 610039, P.R. China*

Jingbo Li − *State Key Laboratory of Infrared Physics, Shanghai Institute of Technical Physics, Chinese Academy of Sciences, Shanghai 200083, P. R. China; University of Chinese Academy of Sciences, Beijing 100049, P. R. China;* orcid.org/0000-0003-1805-9281

https://doi.org/10.1021/acsomega.2c05016
ACS Omega 2022, 7, 36712−36727

Lin Jiang − *State Key Laboratory of Infrared Physics, Shanghai Institute of Technical Physics, Chinese Academy of Sciences, Shanghai 200083, P. R. China; University of Chinese Academy of Sciences, Beijing 100049, P. R. China*

Wei Zhou − *State Key Laboratory of Infrared Physics, Shanghai Institute of Technical Physics, Chinese Academy of Sciences, Shanghai 200083, P. R. China; University of Chinese Academy of Sciences, Beijing 100049, P. R. China;* orcid.org/0000-0002-6050-8311

Yanqing Gao − *State Key Laboratory of Infrared Physics, Shanghai Institute of Technical Physics, Chinese Academy of Sciences, Shanghai 200083, P. R. China; University of Chinese Academy of Sciences, Beijing 100049, P. R. China*

Jingguo Huang − *State Key Laboratory of Infrared Physics, Shanghai Institute of Technical Physics, Chinese Academy of Sciences, Shanghai 200083, P. R. China; University of Chinese Academy of Sciences, Beijing 100049, P. R. China*

Complete contact information is available at: https://pubs.acs.org/10.1021/acsomega.2c05016

Notes

The authors declare no competing financial interest.

■ ACKNOWLEDGMENTS

This work was supported by the National Science Funds (Grants no. 61625505, 12134016), the Chinese Academy of Sciences (Grants no. ZDBS-LY-JSC025), the Sino-Russia International Joint Laboratory of Terahertz Materials and Devices (Grants no. 18590750500), and the Shanghai Municipal Science and Technology Major Project (Grant no.2019SHZDZX01).

■ REFERENCES

(1) Smith, W. J.; Padilla, D. C.; Vier, S. C.; Nemat-Nasser, S.; Schultz, D. R. Composite Medium with Simultaneously Negative Permeability and Permittivity. *Phys. Rev. Lett.* **2000**, *84*, 4184−7.

(2) Pendry, J. B. Negative refraction makes a perfect lens. *Phys. Rev. Lett.* **2000**, *85*, 3966−3969.

(3) Pendry, J. B.; Ramakrishna, S. A. Focusing light using negative refraction. *J. Phys. Condens. Mat.* **2003**, *15*, 6345−6364.

(4) Bilotti, F.; Nucci, L.; Vegni, L. An SRR Based Microwave Absorber. *Microw. Opt. Techn. Let.* **2006**, *48*, 2171−2175.

(5) Zheludev, N. I. The Road Ahead for Metamaterials. *Science* **2010**, *328*, 582−583.

(6) Ma, B.; Liu, S.; Kong, X.; Jiang, Y.; Xu, Y.; Yang, H. A novel wide-band tunable metamaterial absorber based on varactor diode/graphene. *Optik* **2016**, *127*, 3039−3043.

(7) Watts, C. M.; Liu, X.; Padilla, W. J. Metamaterial Electromagnetic Wave Absorbers. *Adv. Mater.* **2012**, *24*, P98−P120.

(8) Smith, D. R.; Pendry, J. B.; Wiltshire, M. C. K. Metamaterials and Negative Refractive Index. *Science* **2004**, *305*, 788−792.

(9) Grant, J.; Ma, Y.; Saha, S.; Khalid, A.; Cumming, D. R. S. Polarization insensitive, broadband terahertz metamaterial absorber. *Opt. Lett.* **2011**, *36*, 3476−3478.

(10) Liang, J.; Zhang, K.; Lei, D.; Yu, L.; Wang, S. Bandwidth-tunable THz absorber based on diagonally distributed double-sized VO_2 disks. *Appl. Optics* **2021**, *60*, 3062.

(11) Xiao, S.; Wang, T.; Liu, T.; Zhou, C.; Jiang, J.; Zhang, J. Active metamaterials and metadevices: a review. *J. Phys. D Appl. Phys.* **2020**, *53*, 503002.

(12) Landy, N. I.; Sajuyigbe, S.; Mock, J. J.; Smith, D. R.; Padilla, W. J. A Perfect Metamaterial Absorber. *Phys. Rev. Lett.* **2008**, *100*, 207402.

(13) Liang, J.; Yu, L.; Wang, Y.; Xue, T.; Lei, D.; Wang, Z.; Li, X. Periodic Arrays of 3D AuNP-Capped VO_2 Shells and Their Temperature-Tunable SERS Performance. *Adv. Opt. Mater.* **2022**, *10*, 2102615.

(14) Bingham, C. M.; Tyler, T.; Jokerst, N.; Smith, D. R.; Padilla, W. J.; Landy, N. I. Design, theory, and measurement of a polarization-insensitive absorber for terahertz imaging. *Phys. Rev. B* **2009**, *79*, 125104.

(15) Tao, H.; Bingham, C. M.; Pilon, D.; Fan, K.; Strikwerda, A. C.; Shrekenhamer, D.; Padilla, W. J.; Zhang, X.; Averitt, R. D. A dual band terahertz metamaterial absorber. *J. Phys. D Appl. Phys.* **2010**, *43*, 225102.

(16) Wen, Q. Y.; Zhang, H. W.; Xie, Y. S.; Yang, Q. H.; Liu, Y. L. Dual band terahertz metamaterial absorber: Design, fabrication, and characterization. *Appl. Phys. Lett.* **2009**, *95*, 207402.

(17) Janneh, M.; De Marcellis, A.; Palange, E.; Tenggara, A. T.; Byun, D. Design of a metasurface-based dual-band Terahertz perfect absorber with very high Q-factors for sensing applications. *Opt. Commun.* **2018**, *416*, 152−159.

(18) Xu, Z.; Gao, R.; Ding, C.; Wu, L.; Zhang, Y.; Xu, D.; Yao, J. Photoexited switchable metamaterial absorber at terahertz frequencies. *Opt. Commun.* **2015**, *344*, 125−128.

(19) Zhang, J.; Wang, G.; Zhang, B.; He, T.; He, Y.; Shen, J. Photo-excited broadband tunable terahertz metamaterial absorber. *Opt. Mater.* **2016**, *54*, 32−36.

(20) Soheilifar, M. R.; Sadeghzadeh, R. A. Design, simulation, and fabrication of an ultrathin planar microwave metamaterial absorber. *Microw. Opt. Techn. Let.* **2015**, *56*, 2916−2922.

(21) Xiong, H.; Zhong, L. L.; Luo, C. M.; Hong, J. S. Dual-band polarization-/angle-insensitive metamaterial absorber. *AIP Adv* **2015**, *5*, 67162.

(22) Tuong, P. V.; Lam, V. D.; Park, J. W.; Choi, E. H.; Nikitov, S. A.; Lee, Y. P. Perfect-absorber metamaterial based on flower-shaped structure. *Photonic. Nanostruct.* **2013**, *11*, 89−94.

(23) Zhou, Y.; Qin, Z.; Liang, Z.; Meng, D.; Xu, H.; Smith, D. R.; Liu, Y. Ultra-broadband metamaterial absorbers from long to very long infrared regime. *Light Sci. Appl.* **2021**, *10*, 138.

(24) Gu, C.; Ma, H.; Qu, S.; Pei, Z.; Xu, Z.; Lin, B.; Zhou, H.; Bai, P.; Gu, W.; Peng, W. Design of a wide-band metamaterial absorber based on resistance films. *Acta Phys. Sin.* **2011**, *60*, 5.

(25) Xie, C.*Electromagnetic fields and electromagnetic waves*, 4nd ed; Higher Education Press: Beijing2006; pp 312-322.

(26) Fu, P.*Research on Metamaterial Terahertz Absorber Based on Graphene*; Tianjin University of Technology, 2019, pp 19−20.

(27) Ye, Y.; Jin, Y. S.; He, S. Omnidirectional, polarization-insensitive and broadband thin absorber in the terahertz regime. *Josa B* **2010**, *27*, 498−504.

(28) Zhou, J.; Economon, E. N.; Koschny, T.; Soukoulis, C. M. Unifying approach to left-handed material design. *Opt. Lett.* **2006**, *31*, 3620−3622.

(29) Zhao, K.; Chen, M.*Electromagnetism*, 2nd ed; Higher Education Press: Beijing, 2006; pp 358-364.

(30) Chen, H. T. Interference theory of metamaterial perfect absorbers. *Opt. Express* **2012**, *20*, 7165−7172.

(31) Zhao, R.; Koschny, T.; Soukoulis, C. M. Chiral metamaterials: retrieval of the effective parameters with and without substrate. *Opt. Express* **2010**, *18*, 14553−14567.

(32) Zhu, W. M.; Liu, A. Q.; Zhang, X. M.; Tsai, D. P.; Bourouina, T.; Teng, J. H.; Zhang, X. H.; Guo, H. C.; Tanoto, H.; et al. Switchable Magnetic Metamaterials Using Micromachining Processes. *Adv. Mater.* **2011**, *23*, 1792−1796.

(33) Song, Y. J.; Sarabandi, K. Equivalent Circuit Model for Metamaterial-Based Electromagnetic Band-Gap Isolator. *IEEE Antennas Wirel. Propag. Lett.* **2012**, *11*, 1366−1369.

(34) Qin, B.; Li, Z.; Hu, F.; Hu, C.; Chen, T.; Zhang, H.; Zhao, Y. Highly Sensitive Detection of Carbendazim by Using Terahertz Time-Domain Spectroscopy Combined With Metamaterial. *IEEE T. Thz. Sci. Techn.* **2018**, *8*, 149−154.

(35) Tong, Y.; Wang, S.; Song, X.; Yang, L.; Yao, J.; Ye, Y.; Ren, Y.; Zhang, Y.; Xin, S.; Ren, X. Multi- band tunable terahertz absorber based on metamaterial. *J. Infrared Millim. W.* **2020**, *39*, 735−741.

(36) Wang, B. X.; Zhai, X.; Wang, G. Z.; Huang, W. Q.; Wang, L. L. A novel dual-band terahertz metamaterial absorber for a sensor application. *J. Appl. Phys.* **2015**, *117*, 2075.
(37) Reynet, O.; Acher, O. Voltage controlled metamaterial. *Appl. Phys. Lett.* **2004**, *84*, 1198−1200.
(38) Gil, I.; García-García, J.; Bonache, J.; Martín, F.; Sorolla, M.; Marqués, R. Varactor-loaded split ring resonators for tunable notch filters at microwave frequencies. *Electron. Lett.* **2004**, *40*, 1347−1348.
(39) Gusynin, V. P.; Sharapov, S. G.; Carbotte, J. P. Magneto-optical conductivity in graphene. *J. Phys. Condens. Mat.* **2007**, *19*, 26221−26222.
(40) Rana, F. Graphene optoelectronics: Plasmons get tuned up. *Nat. Nanotechnol.* **2011**, *6*, 611−612.
(41) Rasoul, A.; Mohamed, F.; Carsten, R.; Falk, L. A perfect absorber made of a graphene micro-ribbon metamaterial. *Opt. Express* **2012**, *20*, 28017−28024.
(42) Yao, G.; Ling, F.; Yue, J.; Luo, C.; Ji, J.; Yao, J. Dual-band tunable perfect metamaterial absorber in the THz range. *Opt. Express* **2016**, *24*, 1518−1527.
(43) He, X.; Yao, Y.; Zhu, Z.; Chen, M.; Zhu, Z.; Yang, W.; Yang, Y.; Wu, F.; Jiang, J. Active graphene metamaterial absorber for terahertz absorption bandwidth, intensity and frequency control. *Opt. Mater. Express* **2018**, *8*, 1031.
(44) Qi, L.; Liu, C. Broadband multilayer graphene metamaterial absorbers. *Opt. Mater. Express* **2019**, *9*, 1298−1309.
(45) Andryieuski, A.; Lavrinenko, A. V. Graphene metamaterials based tunable terahertz absorber: effective surface conductivity approach. *Opt. Express* **2013**, *21*, 9144−9155.
(46) Kaipa, C. S. R.; Yakovlev, A. B.; Hanson, G. W.; Padooru, Y. R.; Medina, F.; Mesa, F. Enhanced transmission with a graphene-dielectric microstructure at low-terahertz frequencies. *Phys. Rev. B* **2012**, *85*, 245401−245407.
(47) Hanson, G. W. Dyadic Green's functions and guided surface waves for a surface conductivity model of graphene. *J. Appl. Phys.* **2008**, *103*, 64301−64302.
(48) Ren, M.; Plum, E.; Xu, J.; Zheludev, N. I. Giant nonlinear optical activity in a plasmonic metamaterial. *Nat. Commun.* **2012**, *3*, 833.
(49) Pershoguba, S. S.; Falkovsky, L. A. Optical far-infrared properties of a graphene monolayer and multilayer. *Phys. Rev. B* **2007**, *76*, 153410.
(50) Zhang, Y.; Li, Y.; Cao, Y.; Liu, Y.; Zhang, H. Graphene induced tunable and polarization-insensitive broadband metamaterial absorber. *Opt. Commun.* **2017**, *382*, 281−287.
(51) Shen, X.; Cui, T. J. Photoexcited broadband redshift switch and strength modulation of terahertz metamaterial absorber. *J. Optics* **2012**, *14*, 114012.
(52) Riccardo, D. I.; David, S. J.; Yash, D. S.; Juraj, S. J.; Piran, R. K.; Stephan, H.; Harvey, E. E. B.; David, A. R. Terahertz optical modulator based on metamaterial split-ring resonators and graphene. *Opt. Eng.* **2014**, *53*, 1−5.
(53) Degl'Innocenti, R.; Jessop, D. S.; Shah, Y. D.; Sibik, J.; Zeitler, J. A.; Kidambi, P. R.; Hofmann, S.; Beere, H. E.; Ritchie, D. A. Low-Bias Terahertz Amplitude Modulator Based on Split-Ring Resonators and Graphene. *ACS Nano* **2014**, *8*, 2548−54.
(54) Sensale-Rodriguez, B.; Yan, R.; Kelly, M. M.; Fang, T.; Tahy, K.; Hwang, W. S.; Jena, D.; Liu, L.; Xing, H. G. Broadband graphene teddrahertz modulatorsenabled by intraband transitions. *Nat. Commun.* **2012**, *3*, 780−781.
(55) Mittendorff, M.; Li, S.; Murphy, T. E. Graphene-Based Waveguide-Integrated Terahertz Modulator. *ACS Photonics* **2017**, *4*, 316−321.
(56) Lee, S. H.; Choi, M.; Kim, T.; Lee, S.; Liu, M.; Yin, X.; Choi, H. K.; Lee, S. S.; Choi, C.-G.; Choi, S.-Y.; Zhang, X.; Min, B. Switching terahertz waves with gate-controlled active graphene metamaterials. *Nat. Mater.* **2012**, *11*, 936−941.
(57) Mao, Q.; Wen, Q.; Tian, W.; Wen, T.; Chen, Z.; Yang, Q.; Zhang, H. High-speed and broadband terahertz wave modulators based on large-area graphene field-effect transistors. *Opt. Lett.* **2014**, *39*, 5649−5652.
(58) Pitchappa, P.; Manjappa, M.; Ho, C. P.; Qian, Y.; Singh, R.; Singh, N.; Lee, C. Active control of near-field coupling in conductively coupled microelectromechanical system metamaterial devices. *Appl. Phys. Lett.* **2016**, *108*, 977.
(59) Ou, J. Y.; Plum, E.; Zhang, J. F.; Zheludev, N. I. An electromechanically reconfigurable plasmonic metamaterial operating in the near-infrared. *Nat. Nanotechnol.* **2014**, *9*, 487.
(60) Wen, Q.; Zhang, H.; Yang, Q.; Xie, Y.; Chen, K.; Liu, Y. Terahertz metamaterials with VO_2 cut-wires for thermal tunability. *Appl. Phys. Lett.* **2010**, *97*, 597.
(61) Yong, Z.; Chen, C.; Xuan, P.; Zhu, Y.; Holtz, M.; Bernussi, A.; Fan, Z. Tuning the properties of VO_2 thin films through growth temperature for infrared and terahertz modulation applications. *J. Appl. Phys.* **2013**, *114*, 113509.
(62) Paul, O.; Imhof, C.; Lägel, B.; Wolff, S.; Heinrich, J.; Höfling, S.; Forchel, A.; Zengerle, R.; Beigang, R.; Rahm, M. Polarization-independent active metamaterial for high-frequency terahertz modulation. *Opt. Express* **2009**, *17*, 819−827.
(63) Chen, H. T.; Padilla, W. J.; Zide, J.; Gossard, A. C.; Taylor, A. J.; Averitt, R. D. Active terahertz metamaterial devices. *Nature* **2006**, *444*, 597−600.
(64) Shrekenhamer, D.; Rout, S.; Strikwerda, A. C.; Bingham, C.; Averitt, R. D.; Sonkusale, S.; Padilla, W. J. High speed terahertz modulation from metamaterials with embedded high electron mobility transistors. *Opt. Express* **2011**, *19*, 9968−9975.
(65) Zhang, Y.; Qiao, S.; Liang, S.; Wu, Z.; Yang, Z.; Feng, Z.; Sun, H.; Zhou, Y.; Sun, L.; Chen, Z.; Zou, X.; Zhang, B.; Hu, J.; Li, S.; Chen, Q.; Li, L.; Xu, G.; Zhao, Y.; Liu, S. Gbps Terahertz External Modulator Based on a Composite Metamaterial with a Double-Channel Heterostructure. *Nano Lett.* **2015**, *15*, 3501.
(66) Zhang, Y.; Zhao, Y.; Liang, S.; Zhang, B.; Wang, L.; Zhou, T.; Kou, W.; Lan, F.; Zeng, H.; et al. Large phase modulation of THz wave via an enhanced resonant active HEMT metasurface. *Nanophotonics* **2019**, *8*, 153−170.
(67) Sun, C.; Sun, B.*Sensing Technology Fundamentals*1nd ed; Publishing House of Electronics Industry: Beijing2001; pp 63-68.
(68) Tonouchi, M. Cutting-edge terahertz technology. *Nat. Photonics* **2007**, *1*, 97−105.
(69) Cai, H. L.; Huang, Q. P.; Hu, X.; Liu, Y.; Fu, Z. P.; Zhao, Y.; He, H. C.; Lu, Y. L. All-Optical and Ultrafast Tuning of Terahertz Plasmonic Metasurfaces. *Adv. Opt. Mater.* **2018**, *6*, 1800143.
(70) Padilla, W. J.; Taylor, A. J.; Highstrete, R. D.; Lee, M.; Averitt, R. D. Dynamical Electric and Magnetic Metamaterial Response at Terahertz Frequencies. *Phys. Rev. Lett.* **2006**, *96*, 107401.
(71) Wen, Q.; Tian, W.; Mao, Q.; Chen, Z.; Liu, W.; Yang, Q.; Sanderson, M.; Zhang, H. Graphene based All-Optical Spatial Terahertz Modulator. *Sci. Rep.* **2014**, *4*, 7409.
(72) Dai, Z.; Yang, J.; Gong, C.; Zhang, N.; Liu, W. Optically controlled graphene based terahertz modulator. *Infrared Laser Eng* **2019**, *48*, 0125001−101250016.
(73) Li, Q.; Tian, Z.; Zhang, X.; Singh, R.; Du, L.; Gu, J.; Han, J.; Zhang, W. Active graphene−silicon hybrid diode for terahertz waves. *Nat. Commun.* **2015**, *6*, 7082.
(74) Savo, S.; Shrekenhamer, D.; Padilla, W. J. Liquid Crystal Metamaterial Absorber Spatial Light Modulator for THz Applications. *Adv. Opt. Mater.* **2014**, *2*, 275−279.
(75) Fekete, L.; Kadlec, F.; Kužel, P.; Němec, H. Ultrafast opto-terahertz photonic crystal modulator. *Opt. Lett.* **2007**, *32*, 680−682.
(76) Chen, H. M.; Su, S.; Wang, J. L.; Zhao, X. Y. Optically-controlled high-speed terahertz wave modulator based on nonlinear photonic crystals. *Opt. Express* **2011**, *19*, 3599−3603.

https://doi.org/10.1021/acsomega.2c05016
ACS Omega 2022, 7, 36712−36727